Cloud radiative forcing at the Atmospheric Radiation Measurement Program Climate Research Facility: 1. Technique, validation, and comparison to satellite-derived diagnostic quantities

Gerald G. Mace,[1] Sally Benson,[1] Karen L. Sonntag,[1,2] Seiji Kato,[3] Qilong Min,[4] Patrick Minnis,[5] Cynthia H. Twohy,[6] Michael Poellot,[7] Xiquan Dong,[7] Charles Long,[8] Qiuqing Zhang,[1] and David R. Doelling[9]

Received 28 February 2005; revised 24 August 2005; accepted 2 December 2005; published 7 June 2006.

[1] It has been hypothesized that continuous ground-based remote sensing measurements from collocated active and passive remote sensors combined with regular soundings of the atmospheric thermodynamic structure can be combined to describe the effects of clouds on the clear sky radiation fluxes. We critically test that hypothesis in this paper and a companion paper (part 2). Using data collected at the Southern Great Plains (SGP) Atmospheric Radiation Measurement (ARM) site sponsored by the U.S. Department of Energy, we explore an analysis methodology that results in the characterization of the physical state of the atmospheric profile at time resolutions of 5 min and vertical resolutions of 90 m. The description includes thermodynamics and water vapor profile information derived by merging radiosonde soundings with ground-based data and continues through specification of the cloud layer occurrence and microphysical and radiative properties derived from retrieval algorithms and parameterizations. The description of the atmospheric physical state includes a calculation of the clear and cloudy sky solar and infrared flux profiles. Validation of the methodology is provided by comparing the calculated fluxes with top of atmosphere (TOA) and surface flux measurements and by comparing the total column optical depths to independently derived estimates. We find over a 1-year period of comparison in overcast uniform skies that the calculations are strongly correlated to measurements with biases in the flux quantities at the surface and TOA of less than 6% and median fractional errors ranging from 12% to as low as 2%. In the optical depth comparison for uniform overcast skies during the year 2000 where the optical depth varies over more than 3 orders of magnitude we find a mean positive bias of less than 1% and a 0.6 correlation coefficient. In addition to a case study where we examine the cloud radiative effects at the TOA, surface and atmosphere by a middle latitude cyclone, we examine the cloud top pressure and optical depth retrievals of ISCCP and LBTM over a period of 1 year. Using overcast periods from the year 2000, we find that the satellite algorithms tend to compare well with data overall but there is a tendency to bias cloud tops into the middle troposphere and underestimate optical depth in high optical depth events.

Citation: Mace, G. G., et al. (2006), Cloud radiative forcing at the Atmospheric Radiation Measurement Program Climate Research Facility: 1. Technique, validation, and comparison to satellite-derived diagnostic quantities, *J. Geophys. Res.*, *111*, D11S90, doi:10.1029/2005JD005921.

1. Introduction

[2] The Atmospheric Radiation Measurement (ARM) program was initiated in the early 1990s with a goal of improving the parameterization of clouds in GCMs [*Stokes and Schwartz*, 1994; *Ackerman and Stokes*, 2003]. A primary contribution of the ARM program has been to continuously document the vertical distribution of clouds,

[1]Department of Meteorology, University of Utah, Salt Lake City, Utah, USA.
[2]Now at Cooperative Institute for Mesoscale Meteorological Studies, University of Oklahoma, Norman, Oklahoma, USA.
[3]Center for Atmospheric Sciences, Hampton University, Hampton, Virginia, USA.
[4]Atmospheric Sciences Research Center, State University of New York, Albany, New York, USA.
[5]NASA Langley Research Center, Hampton, Virginia, USA.
[6]College of Oceanic and Atmospheric Sciences, Oregon State University, Corvallis, Oregon, USA.
[7]Department of Atmospheric Sciences, University of North Dakota, Grand Forks, North Dakota, USA.
[8]Pacific Northwest National Laboratory, Richland, Washington, USA.
[9]Analytical Services and Materials, Inc., Hampton, Virginia, USA.

0148-0227/06/2005JD005921

the associated thermodynamic states, and the effect of clouds on the surface radiation budget at a few highly instrumented sites. The ARM program began at about the time of several intensive field programs known as the First ISCCP Regional Experiments (FIRE) that were conducted in the late 1980s and the early 1990s [*Randall et al.*, 1995]. The case study approach of the FIRE deployments was fruitful in that a great deal was learned about the properties of cirrus and stratus clouds [*Stephens*, 1995; *Randall*, 1995]. What was missing from these experiments was sufficient statistical breadth to determine how the knowledge gained from the case studies could be generally applied to the atmosphere in the form of GCM parameterizations. This difficulty was recognized, and the ARM planners speculated that a long-term field project approach could complement short-term intensive studies. While the ARM observational paradigm lacks the global nature of a satellite-based program, it is complementary in that the sheer continuity and breadth of the continuous multiyear ground-based data ensures that, given sufficient time, a statistically significant sample of the accessible climate states for a particular region will be observed at a ground site, i.e., the ergodic hypothesis [*Peixoto and Oort*, 1993]. The ARM data set exists in a fairly raw form, however. Even though the data are continuously collected, quality controlled, routinely calibrated, and made freely available to the scientific community, converting the observations into descriptions of cloud properties and radiative heating is a specific challenge that we address here.

[3] In this paper, we describe a data analysis technique that attempts to reduce the raw ARM data into a meaningful description of the atmospheric physical state. Our motivation for pursuing this goal is the assumption that simultaneous knowledge of the cloud properties, and the large-scale meteorology (i.e., those scales of motion that can reasonably be resolved by a climate model), along with their statistics, over extended time periods can lead to an improved understanding of the coupling between the large-scale meteorology and the radiative feedbacks to the atmospheric circulation. In this paper and a companion paper [*Mace et al.*, 2006, hereinafter referred to as part 2] we examine the cloud radiative forcing of the atmosphere as a function of cloud type at the ARM Southern Great Plains (SGP) central facility (SCF) near Lamont, Oklahoma during the year 2000 with special emphasis on the month of March. In the next section, we describe the data analysis procedure and validation of the results using TOA and surface cloud radiative observations. In section 3, we conduct a direct comparison of the cloud top pressure and total column optical depth with similar quantities produced by the International Satellite Cloud Climatology Product (ISCCP [*Rossow and Zhang*, 1995]) and by an analysis of Geostationary Operational Environmental Satellite (GOES) data [*Minnis et al.*, 1993, 1995]. In part 2 we consider the evolution of the synoptic-scale atmosphere over the central United States during March 2000 and the coupling between the synoptic state, the cloud types, and the radiative feedbacks that were observed at the SCF, and we examine the radiative feedbacks to the atmosphere as a function of cloud type.

2. Technique

[4] We begin this section with a discussion of the data streams that are particularly important to our characterization of the atmospheric state, and then we describe a methodology to merge these raw individual data streams into a reasonably complete time-dependent description of the atmospheric column over the SCF. During this discussion, we use for illustration the period from 1–3 March 2000. During this period a deep middle latitude cyclone passed over the SGP region. Figure 1 shows the evolution of the 500 mb height and vorticity field during this period beginning with a migratory ridge followed by a closed low that moved over the SGP from the southwestern U.S. Satellite imagery in Figure 2 shows that cirrus upstream of the 500 mb ridge on 1 March gave way to a deep cloud system on 2 March followed by a large area of boundary layer clouds with some higher clouds. This period marked the beginning of a multiweek intensive observational campaign at the SCF when multiple aircraft and several additional ground-based instruments were assembled to investigate the three dimensional properties of clouds that passed through the region.

[5] The ARM data that we consider consist of measurements from several independently operating instruments situated in a cluster at the SCF. These instruments nominally operate on a continuous basis, the data streams go through separate routine calibration and quality control procedures, and the data are eventually made freely available in an archive facility. Since the data are stored in a fairly raw form (temporally resolved files of geophysical measurements and metadata from particular instruments), the data are not immediately amenable, with a few exceptions, to describing the physical properties of the atmosphere. Remote sensors, for instance, are often sensitive to certain aspects of the atmosphere that may require interpretation. Radar, for instance, is sensitive to the sixth moment of the particle size distribution while the third moment is most descriptive of condensed mass and the second moment of optical extinction. Even lidar measurements, which are sensitive to the second moment of the cloud particle size distribution, are modulated by two-way extinction and multiple scattering. Our task is to combine the raw ARM data into a consistent entity that lends itself to describing the time evolving physical state of the column, a description that practitioners of mesoscale or large-scale models could use for comparison with minimal additional processing. While this task eventually reduces to estimating cloud microphysical and radiative properties, the initial data processing we undertake should be addressed briefly. See Appendix A for more detail.

[6] The initial data processing has two essential goals. The first is to characterize the continuous thermodynamic state of the atmospheric column and the second is to use the active remote sensors to identify the locations of cloud. While ARM has devoted considerable resources to launching radiosondes from the SCF and from several boundary facilities, the record is not continuous. Only during IOPs are radiosondes launched at 3-hourly intervals 24 hours per day. At other times the schedule is less regular. Furthermore, other data sources such as continuous ground-based meteorological information and measurements of the water vapor path from the microwave radiometer are continuously available. Therefore we have developed a simple scheme to routinely combine available radiosondes with other more continuous measurements.

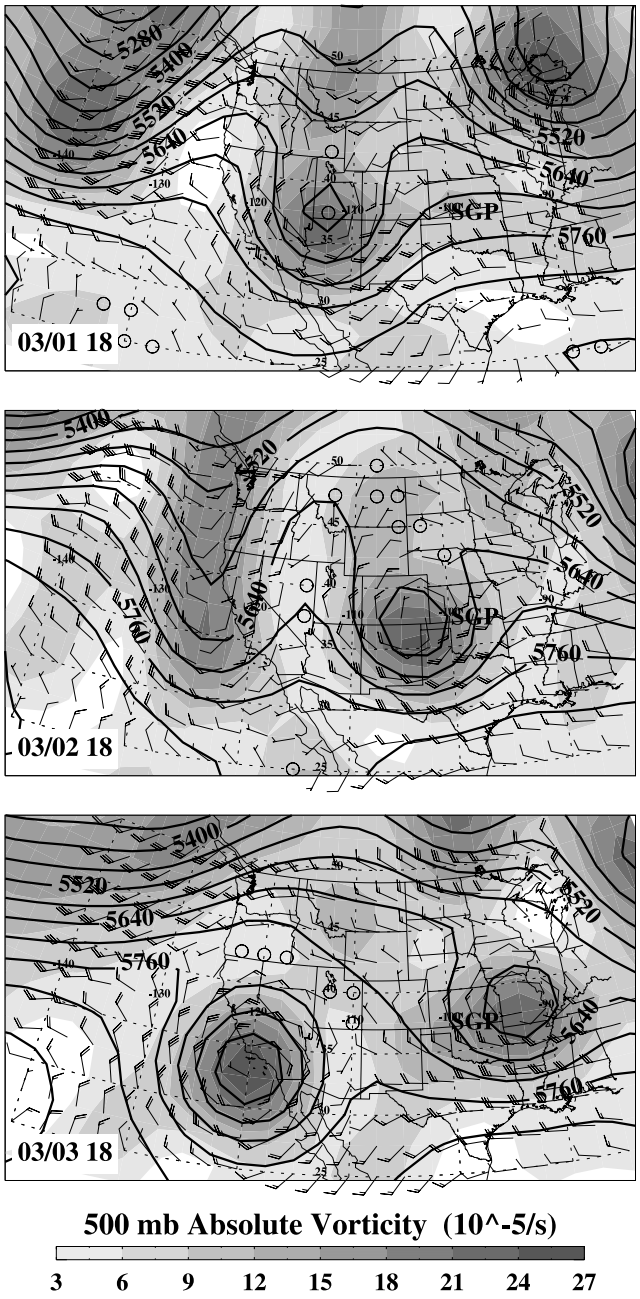

Figure 1. The 500 mb heights (contours in m), abs vorticity (shaded), and horizontal wind (one whole barb is 10 m/s) from the NCEP/NCAR reanalysis for the 1–3 March 2000 case study period. The date (month/day) and UTC time is shown on the bottom left of each plot.

[7] The millimeter cloud radar (MMCR) data are also processed beginning with the Doppler moments. Because the MMCR cycles through several modes to optimize sensitivity taking a total of 36 s for one cycle, it is important that the data from the individual modes are carefully screened and then combined. We follow a technique similar to that described by *Clothiaux et al.* [1995] to identify significant return in the data. We then combine the cloud measurements with the thermodynamics on a height-time grid that has 90 m and 5 min resolution. For most variables such as the Doppler moments, averaging is performed in time. For quantities that are only defined in clouds (such as radar reflectivity), we average only those observations during a 5 min period deemed to be associated with clouds by the cloud mask and we store the number of actual cloud occurrences in the 5 min period along with the number of possible occurrences for later consideration. This 5 min and 90 m time series forms the basis of what we term the column physical characterization (for convenience, we hereinafter refer to this as the CPC). Additional details on the data reduction can be found in Appendix A.

[8] Figures 3 and 4 show the microwave radiometer measurements and the thermodynamics derived for the case study period (1–3 March) while Figure 5 illustrates the MMCR data. We find that a highly variable layer of cirrus was observed by the MMCR beginning on the afternoon of 1 March that appears to have passed over the radar in 4–5 distinct pulses. The layers deepened to be 3–4 km thick and were capped at the tropopause with each pulse lasting 2–3 hours followed by a 1–2 hour separation. Following the final cirrus episode, a deep cloud system that marked the advancing middle latitude front and low-pressure system was observed by the MMCR. Rain began at approximately 1100 UTC on 2 March and persisted until just after 2000 UTC on 2 March with a break in precipitation between 1630 and 1830 UTC. The precipitation periods as diagnosed from an empirical technique applied to microwave radiometer data (described in Appendix A) is shown as a background light red on the radar height-time figure. Note that a radar bright band can be observed during this period of heavy cloud cover and precipitation. It is interesting to note the close correspondence between the radar time series and the features in the satellite imagery.

[9] The deep clouds that passed over the radar prior to 1630 UTC on 2 March were followed by a transition to a layer of clouds based in the boundary layer that had tops near 4 km along with scattered cirrus that is plainly visible on the 1830 UTC 2 March satellite image. The heavy clouds with rain that moved over the SCF after 1900 UTC on 2 March can be identified in the satellite image as the region of low brightness temperatures just southwest of the SCF at 1830 UTC. The cloud layer thinned considerably after 2100 UTC and was predominantly a boundary layer cloud layer. While disturbances rotated around the vortex, the low-pressure center passed just north of the SCF at around 1200 UTC. One of these disturbances resulted in deeper clouds and a period of light rain as it passed over the SCF between 0600 and 0900 UTC on 3 March. The cold sector of the cyclone brought occasional cirrus over a general boundary layer overcast during the day on 3 March. This period has been a focus of study since the NASA ER2 flew a mission under the newly launched Terra satellite that passed nearly overhead at 1735 UTC while the University of North Dakota Citation sampled the boundary layer clouds in situ [*Dong and Mace*, 2003; *Dong et al.*, 2002].

2.1. Cloud Microphysical and Radiative Properties

[10] The goal of creating a continuous record of cloud microphysics with ARM data has been longstanding but difficult to achieve. While algorithms have been developed to treat specific cloud types such as thin cirrus [*Mace et al.*, 1998, 2002; *Matrosov et al.*, 1994] and boundary layer

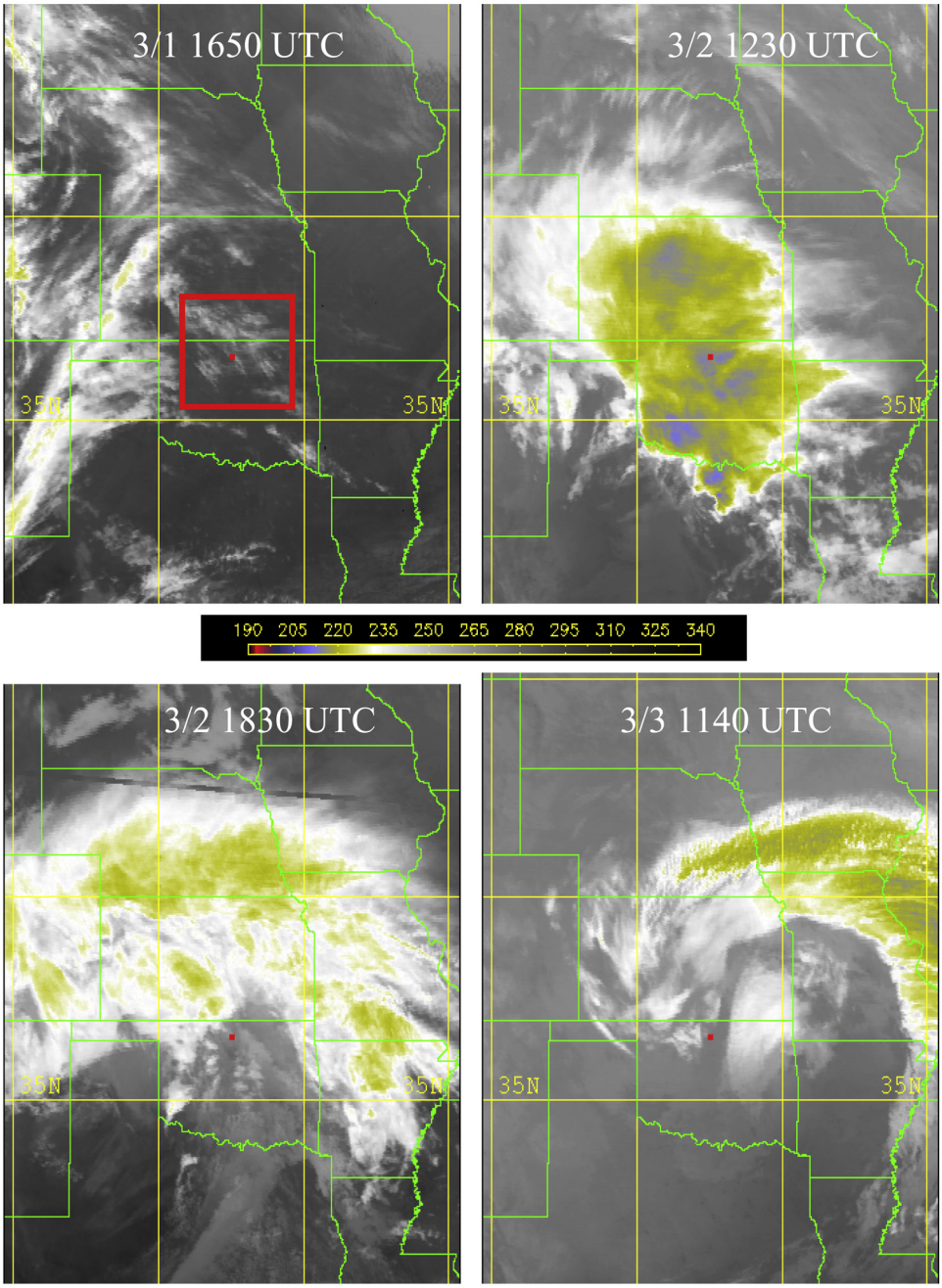

Figure 2. IR Geostationary satellite imagery of the ARM SGP region during the 1–3 March case study period. The location of the ARM SCF is marked with a red dot. State outlines are shown in green and latitude and longitude lines are shown in yellow. The color table is denoted in Kelvins.

liquid-phase clouds [*Frisch et al.*, 1995, 1998; *Mace and Sassen*, 2000; *Dong and Mace*, 2003]. developing algorithms to treat clouds generally with objective algorithms continues to be an active research topic. While cloud properties derived from existing algorithms can be used where applicable, to achieve our objective, a more general approach is required. We use cloud property retrievals when possible, but do not limit our analysis of cloud radiative properties to the periods when retrieval results are available. What we describe in this section is an approach to this problem that attempts to temporarily circumvent the current technological limitations where we use an ad hoc combination of algorithms, parameterizations, and empirical relationships. The scheme is necessarily modular and allows for insertion of additional algorithms as they are developed and shown to be superior to what is currently used. It is important to understand that what we describe below is a first approximation, a baseline, against which new retrieval techniques can be tested and implemented as they are developed.

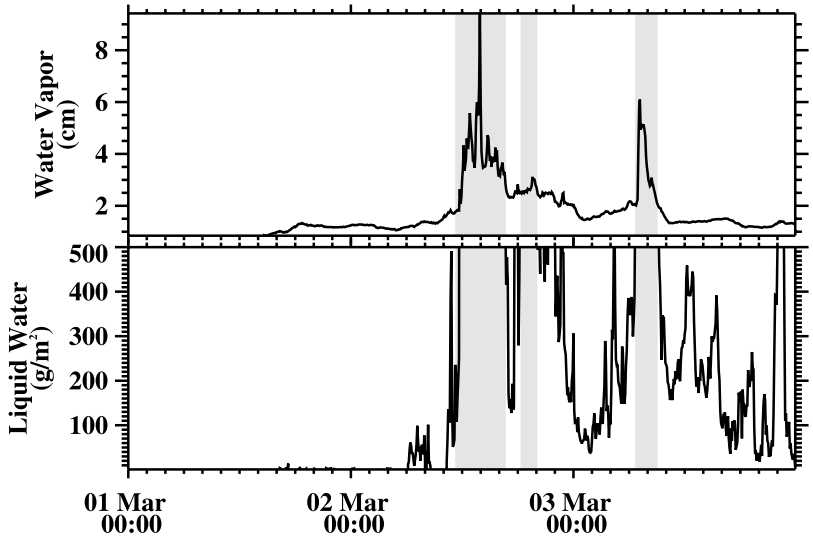

Figure 3. MWR observations and wet window flag for the 1–3 March 2000 case study period. The shaded regions denote periods where the empirical algorithm identifies a high likelihood that condensed liquid water on the instrument cover biased the MWR measurements.

[11] To derive a generalized cloud property description it is useful to recognize what information we have directly from observations, what cloud properties can be retrieved in a straightforward way from the observations, what cloud properties can be retrieved from algorithms, and which cloud properties need to be developed from parameterizations. We know the cloud layer bases and tops, the temperatures of the cloud layers, and the vertically integrated liquid water content (LWP). This information greatly constrains the microphysical and radiative properties of the column. What we don't know is how the LWP should be distributed vertically; we have no direct information on the distribution of ice water either in an integrated or vertically resolved sense; and we have no direct information on particle size.

[12] The critical issue that must be addressed is related to the use of the radar reflectivity and Doppler velocity as quantities that contain information about condensed water and particle size. In nonprecipitating liquid or ice phase volumes where the particles are small with respect to the 8mm wavelength of the MMCR, the radar reflectivity provides information on the square of the water content [*Frisch et al.*, 1998] while for volumes that contain large ice crystals perhaps coincident with liquid water, the radar reflectivity, because it is principally derived from the largest particles, provides information primarily on the condensed mass of the ice phase leaving us with very little information about the liquid phase. The empirical relationships we require, therefore, must provide information on the normalized distribution of liquid water in the vertical column so that we can (1) distinguish between that portion of the LWP derived from warm (i.e., temperature greater than freezing) cloud volumes and that portion derived from supercooled cloud volumes and (2) distribute the supercooled LWP vertically. *Kiehl et al.* [1998] provides such a parameterization that was derived for use in the Community Climate Model from other empirical data. The Kiehl et al. parameterization provides for exponentially decreasing water content with decreasing temperature. This ensures that the supercooled portion of cloudy columns will have much less water path than those portions warmer than freezing. In future implementations, we will develop a database of such relationships segregated by meteorological type derived from ensemble runs of a cloud-resolving model. It is important to realize, however, that we use the parameterized profile of LWC only in a vertically normalized sense to provide information on how to distribute the measured LWP within the actual cloud layers observed by the MMCR.

[13] In that portion of the profile where temperatures are warmer than freezing and clouds are observed by the MMCR, we distribute the warm fraction of the LWP vertically using the *Frisch et al.* [1998] parameterization where the normalized square root of the radar reflectivity is used as a vertical weighting function. In the region of the profile where supercooled clouds are observed by the MMCR and are not cirrus layers (see below), we distribute the supercooled fraction of the LWP vertically according to the empirical distribution function of liquid water within the hydrometeor layers observed by the MMCR. In other words, we have an estimate of the supercooled water path and we know the layer boundaries of the supercooled layers. The parameterization is used simply as a weighting function to distribute that water within the appropriate cloud layers. The particle sizes of the warm liquid phase volumes are then calculated using a simple expression for effective radius derived from aircraft data and analytical considerations by *Dong and Mace* [2003]: $r_{e,liq} = 19.5 \exp(0.034\, dBZ_e)$ where dBZ_e is $10\log_{10} Z_e$. This expression is assumed valid for $r_{e,liq} < 10$ μm. Effective radii that are diagnosed to be greater than 10 μm are assumed to be possibly contaminated by precipitation and the cloud particle effective radii are set to 10.0 μm. For the liquid phase clouds that exist at temperatures colder than freezing, we assume that $r_{e,liq} = 15$ μm.

[14] For cloud ice water content (IWC), we face a more difficult challenge since no integral constraint exists for the total column mass. Cirrus clouds, defined as layers dominated by ice microphysical processes in the upper troposphere, are identified on the basis of a thermodynamic and

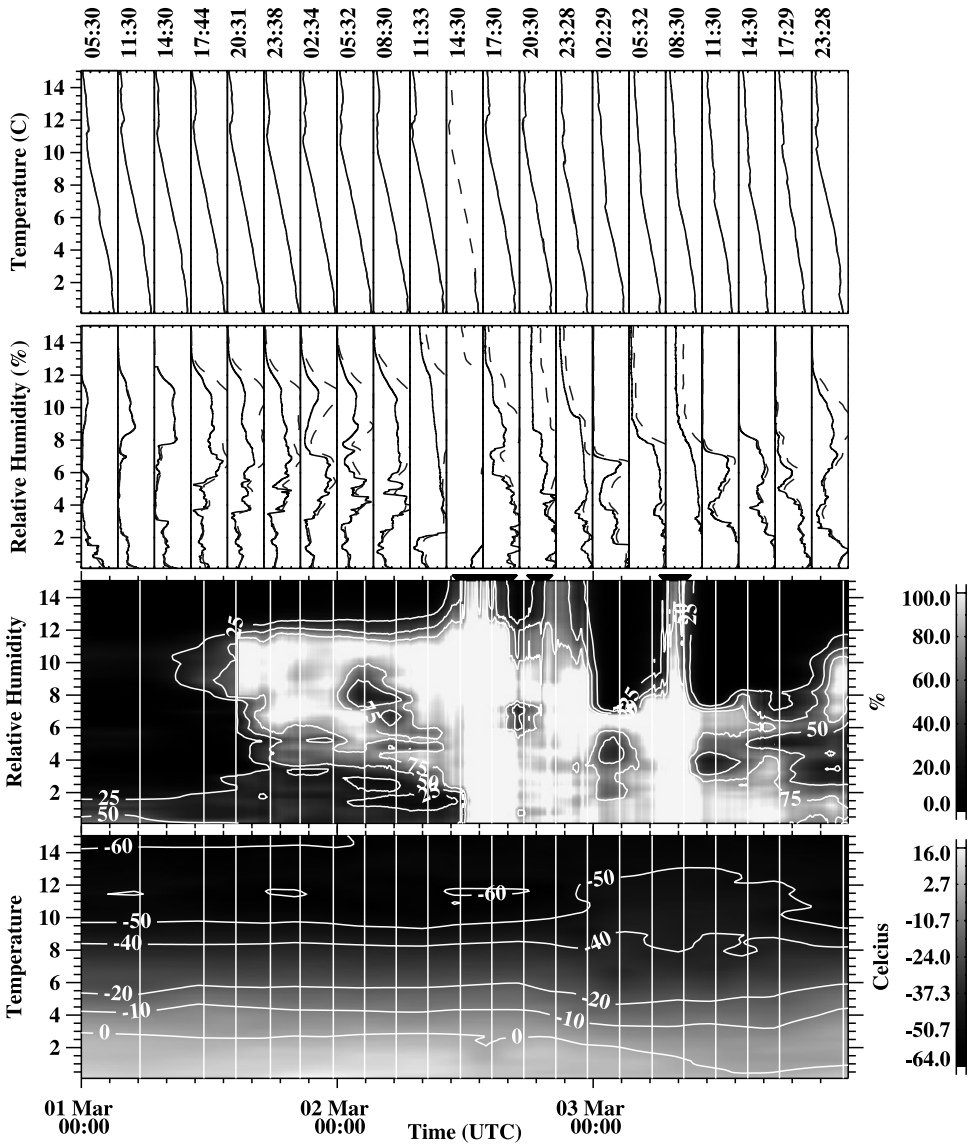

Figure 4. Illustration of the thermodynamic fields derived from 3-hourly radiosondes and MWR liquid water path during the 1–3 March 2000 case study period. The top two plots show the interpolated values (dashed lines) compared to the soundings (solid) while the bottom two plots show the interpolated fields at 5 min resolution. The heavy black symbols above the Relative Humidity height-time cross section show periods where the MWR liquid water path was likely contaminated by liquid water on the MWR cover (see Figure 3).

radar reflectivity-based definition discussed by *Mace et al.* [2001]. We use a hierarchy of algorithms starting with the approach described by *Mace et al.* [2002] that uses the radar reflectivity and the Doppler velocity (hereinafter referred to as the Z-V algorithm) and returns a profile of IWC and particle size. Since the Z-V algorithm cannot always be applied because of strong vertical air motions, we use results derived by combining radar reflectivity and downwelling IR radiance (Z-R algorithm [*Mace et al.*, 1998, 2005]) that provides IWP and layer-mean effective size. If neither the Z-V algorithm nor Z-R algorithm results are available, we use the temperature-dependent regression equations provided *Liu and Illingworth* [2000] for middle latitude cirrus. When the Liu and Illingworth parameterization is used, the cloud particle size for cirrus is parameterized using the simple pressure-dependent effective radii expression described by *Kiehl et al.* [1998]. Since these algorithms were developed independently, are based on different assumptions, and have very different and perhaps not well understood error characteristics, we occasionally find unphysical gradients in cloud microphysical properties when transitioning between algorithms. We do not attempt to smooth these gradients in any way since our goal is to provide the best estimate of the cloud property at a given point in time although we do keep track of what algorithm is supplying what property at all times. As our skill in deriving cloud properties from remote sensing data improves, we anticipate that the solutions from various algorithms will converge.

[15] Ice phase volumes that cap deeper cloud layers such as nimbostratus or cloud volumes that may be mixed phase (i.e., thick altostratus, altocumulus, nimbostratus, and cold

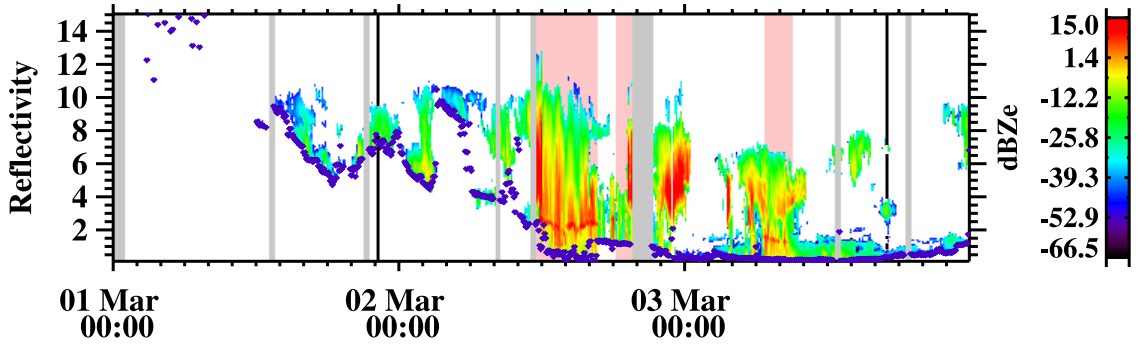

Figure 5. MMCR radar reflectivity of cloud layers during the 1–3 March 2000 case study period. The red-shaded regions mark periods when the MWR cover was identified as likely wet, the gray shaded regions denote missing data, and the two black lines through the data at 2215 UTC on 1 March and 1715 UTC on 3 March denote profiles that are examined in more detail.

boundary layer clouds) are a more difficult problem since there has been relatively little observational treatment relating ice mass and radar reflectivity in these clouds. Aside from the thermodynamics, the routine ARM observations of such clouds are limited to the MMCR Doppler moments. Ultimately, physically based cloud property retrieval algorithms are needed. However, no such algorithms are in common use at this time. Therefore our goal is to develop a reasonable approximation of the properties of these clouds using available data in lieu of results from physically based algorithms. In developing this parameterization, we assume that the radar measurements are primarily derived from the ice phase at temperatures colder than freezing. This assumption could cause biases in total water where the ice phase has not been initiated above the freezing level.

[16] Using a multiple linear regression approach we seek a function of the form,

$$\log_{10} IWC = a + b \log_{10} (F_1(Z_e, V_d)) + cF_2(T) \qquad (1)$$

where V_d is the Doppler velocity and T is temperature. Equation (1) can be simplified and written $IWC = a_i(T)F_1(V_d, Z_d)^b$ where $a_i = 10^{a+cF_2(T)}$ which has an approximate form of a temperature-dependent *Z-IWC* power law modified by the Doppler velocity. Our initial goal is to find functions F_1 and F_2. Neglecting air motions, the Doppler velocity is a volume-average ensemble particle fall speed weighted by the radar reflectivity, while the terminal velocity of an individual ice particle is determined primarily by the ratio of the particle mass to its area [*Heymsfield*, 1972; *Mitchell*, 1996; *Heymsfield et al.*, 2002; *Mitchell and Heymsfield*, 2005]. As derived in Appendix B, $F_1(V_d, Z_e)\} \cong IWC = C\ Z_e\ V_d^{-\alpha}$ where C and α depend on the coefficients of power law relationships describing particle mass, area, and fallspeed in terms of particle maximum dimension. Since this parameterization is to be implemented in middle tropospheric clouds, we assume power law coefficients that have low mass and high area as listed by *Mitchell* [1996, Table 1]. With this assumption, $C = 6.68 \times 10^{-6}$ and $\alpha = 1.2$ with all units cgs. While our expression for $F_1(V_d, Z_e)$ does return an estimate of the *IWC*, the set of power law coefficients that determine C and α for any given case are not well known in middle tropospheric ice and mixed-phase clouds and almost certainly change from case to case. Therefore we seek to add additional information to the parameterization using the temperature of the cloud volume under consideration and then allow for empirical adjustments of the *IWC* estimates through regression against observations. While we expect the *IWC* to be related to the temperature [*Heymsfield and Platt*, 1984], we expect that a more linear relationship would exist between the condensed mass and a quantity proportional to the temperature-dependent equilibrium vapor pressure. So, we set $F_2(T) = \exp\left[\frac{L}{R_v}\left(\frac{1}{273} - \frac{1}{T}\right)\right]$ where L and R_v are the latent heat of sublimation and the gas constant for water vapor, respectively.

[17] To derive the coefficients, a, b, and c, in equation (1) we use the in situ microphysical data set that was collected by the University of North Dakota Cessna Citation during the March 2000 intensive observation period (IOP). For the present application, we use data collected in middle tropospheric mixed and ice-phase layers on 12, 13, 17, 18, and 21 March. The instrument complement on the Citation included the standard Particle Measurement Systems 2DC to characterize a portion of the particle size distribution from approximately 100 μm to 1000 μm and the Counterflow Virtual Impactor (CVI [*Twohy et al.*, 1997]) to directly measure the condensed mass. The counter flow of the CVI during this IOP excluded particles with diameter smaller than 7 to 9 μm. In mixed-phase conditions, significant liquid could exist because of particle sizes larger than this minimum size. Since we are interested in the ice mass, we use the King liquid water probe to determine when liquid exists, and then subtract from the CVI observation the fraction of the King liquid water content that is due to particle sizes larger than 7 microns as determined by integrating the Forward Scattering Spectrometer Probe size distributions (the FSSP is sensitive to small sizes from a few microns to 50 microns). This procedure assumes that the FSSP senses primarily liquid water droplets and that no significant fraction of the IWC exists at sizes smaller than the minimum size of the CVI.

Table 1. Coefficients of the Regression Relationship (Equation (1)) Relating Z_e (mm^6 m^{-3}), V_d (m s^{-1}), and T (K) to *IWC* (g cm^{-3})

	Coefficient
a	−2.35
b	0.639
c	−7.16e−5

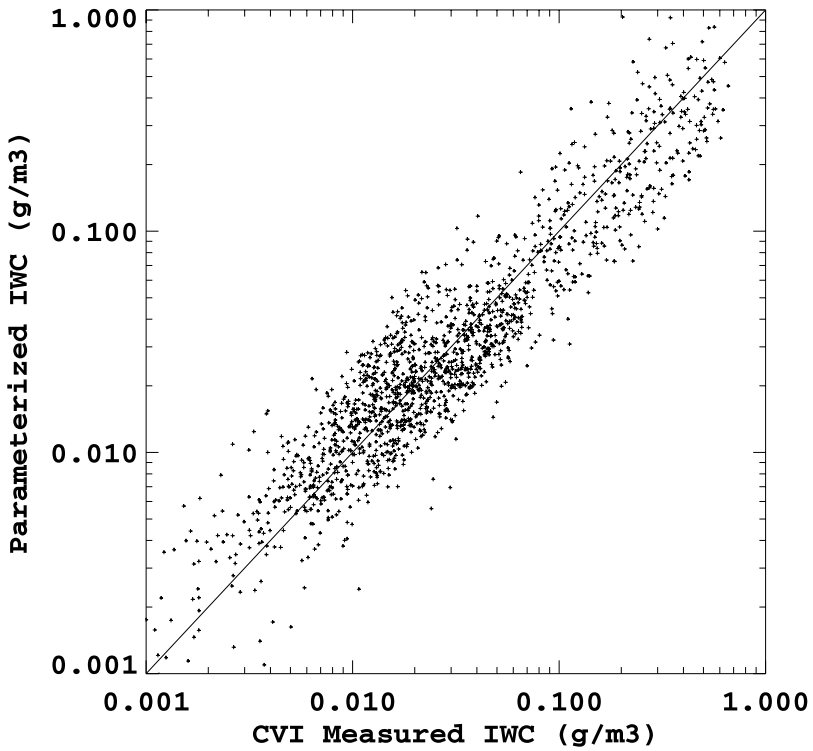

Figure 6. Comparison of IWC derived from the equation (1) regression relationship to CVI measurements of condensed water. See text for further details.

[18] Using a bimodal functional fit to the 5-s averaged 2DC size spectra to approximate the full particle size distribution [*Mace et al.*, 2002], we calculate a value for the radar reflectivity using the approach outlined by *Atlas et al.* [1995] and then calculate the Doppler velocity by combining the bimodal functional approximation of the size distribution and the area and mass measurements provided by the 2DC and CVI [*Heymsfield et al.*, 2002]. The calculated Z_e and V_d, the CVI IWC and the temperature measured by the Citation are used in a multiple linear regression algorithm to derive the coefficients for equation (1) (see Table 1). Since the particle size spectra from the 2DC are known to have large uncertainties and do not fully resolve the size spectrum that could be encountered in these clouds, we expect significant uncertainty in the calculated radar reflectivity and Doppler velocity. The CVI mass measurements can also have substantial uncertainty (~15%). Therefore, to remove outlying data points, the measurements are compared to a *Z-IWC* relationship published by *Heymsfield* [1977] in an extensive analysis of midlatitude deep ice-phase clouds where the relationship $IWC = 0.035Z^{0.505}$ was found. We discard any data whose *Z-IWC* combination is more than a factor of 3 outside of this relationship; thus the filter only excludes true outliers. After processing and filtering data from the flights listed above, we are left with approximately 1500 5-s averages of *IWC*, *T*, and calculated Z_e and V_d. Figure 6 and Table 2 demonstrate that the regression-based algorithm reasonably approximates the observed IWC in terms of Z_e, V_d, and *T*. The correlation coefficient of the derived IWC compared to the observations is 0.85 with a bias of 0.4 mg m^{-3} (the mean IWC in this data set is 64 mg m^{-3}) and median error of 32%. Finally, the particle size of the ice-phase in these clouds is parameterized using the *Kiehl et al.* [1998] parameterization.

[19] The diagnosed condensed water for the 1–3 March period is shown in Figure 7. While for continuity we show the diagnosed liquid water in the periods when precipitation was occurring (background shaded light pink), the liquid water content and path at these times are overestimates because the MWR radome was wet and therefore biased high by emission from condensed water on the radome. The cirrus field on 1 and 2 March that passed over the SGP in the southwesterly flow ahead of the low-pressure system is estimated to have had IWP ranging up to about 100 gm^{-2} in the thicker portion near 0300 UTC. As the deep cloud structure advanced over the SCF associated with the deepening weather system, precipitation began almost immediately. The IWP during the period as derived from the regression parameterization is estimated to be several hundred g m^{-2}, the MWR-derived LWP is not valid, however,

Table 2. Comparison Statistics of the Parameterized Versus Observed *IWC* Derived From Equation (1) and Table 1 and Shown in Figure 6

Statistic	Value
Bias, g m^{-3}	−0.004
Median fractional error	0.32
Slope of linear fit	0.85
Intercept of linear fit, g m^{-3}	0.006
Correlation coefficient	0.85
Normal deviation, g m^{-3}	0.06
Number of observations	1562

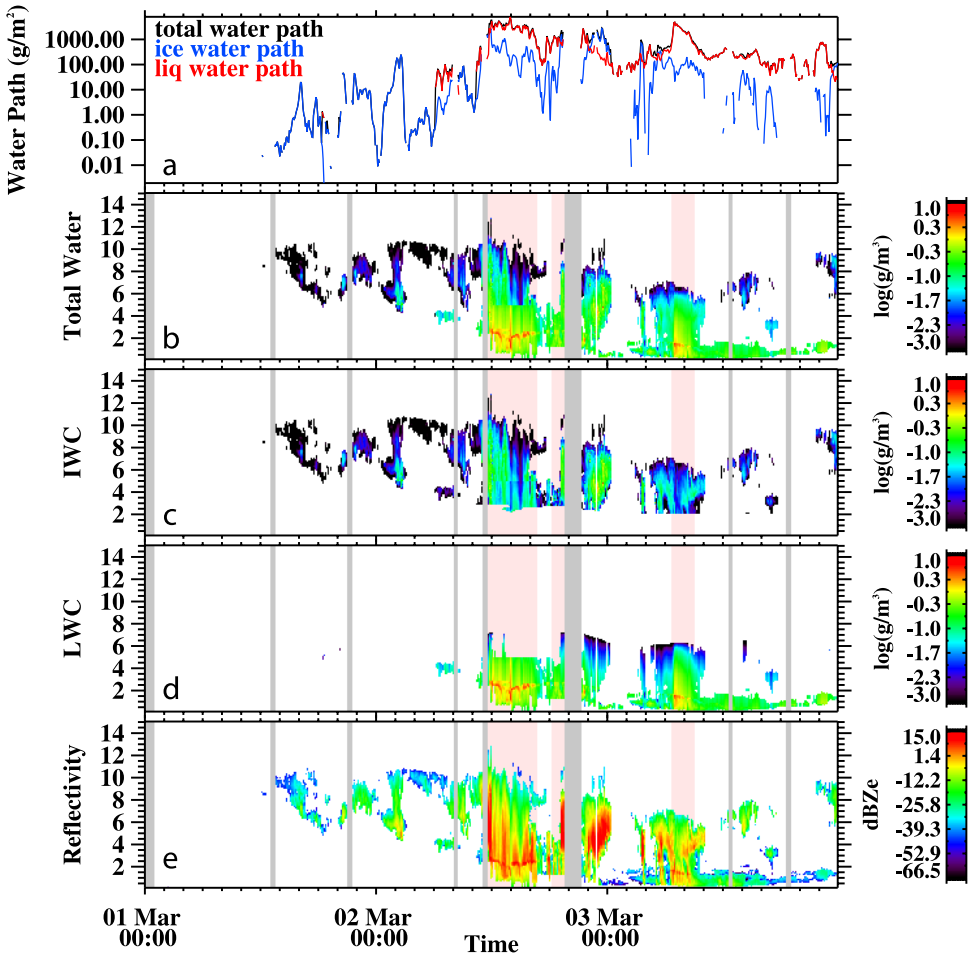

Figure 7. Condensed water derived from the CPC algorithm for the 1–3 March case study period. (a) Total, liquid, and ice water paths, (b) height-time section of total condensed water, (c) IWC, (d) LWC, and (e) radar reflectivity observed by the MMCR. Light red shading denotes regions where the MWR is likely biased because of a wet cover. The LWC and total water should be viewed with caution during these times. Gray shaded areas denote missing data.

because of rain on the MWR radome. The brief period between rain events on 2 March when cirrus was observed above a lower layer that existed between 2 and 5 km had total water path near 600 gm^{-2} with just 100 gm^{-2} of that amount due to ice with most of the IWP in the mixed phase portion of the lower layer. The behavior of the condensed water algorithm described above is evident in the various derived features of the cloud field on 3 March. The boundary layer cloud was always warmer than freezing and the high cirrus features were estimated to be all ice. The cloud feature that passed over the SCF between 1700 and 1800 UTC between 4 and 5 km was in the temperature range between 274 and 260 K and was deemed to be mixed phase. Note that the microwave radiometer retrieval of LWP shows a definite increase between 1700 and 1800 UTC that does not appear to correspond to an increase in the radar reflectivity of the stratocumulus in the boundary layer.

2.2. Radiative Properties and Radiative Fluxes

[20] With an estimate of the microphysical properties of the profiles, published parameterizations are used to estimate the radiative properties of the cloudy volumes. These parameterizations depend typically on the condensed water content and some measure of effective particle size. For the shortwave radiative properties of condensed liquid, the parameterization described by *Slingo* [1989] is used, and the simple radiative parameterization described by *Kiehl et al.* [1998] is used for the longwave radiative properties of the liquid phase. For the ice phase, we use the *Fu* [1996] and *Fu et al.* [1998] parameterizations for the shortwave and longwave radiative properties, respectively. The cloud radiative properties are then combined with the radiative properties of the clear atmosphere to calculate the profiles of solar and longwave radiative fluxes. The radiative transfer model uses a two-stream approximation given by *Liou* [1974] and the solution algorithm is developed by *Toon et al.* [1989]. The k-distribution method described by *Kato et al.* [1999] with the correlated-k assumption provides estimates of the gaseous absorption optical thickness of water vapor, ozone, carbon dioxide, and oxygen in the shortwave spectral region using 32 spectral intervals between 0.25 and 4.5 μm [*Kato et al.*, 2001]. In the longwave, the radiative properties of the gaseous constituents (including O_3, H_2O, N_2O, and CH_4) are derived using the approach described by

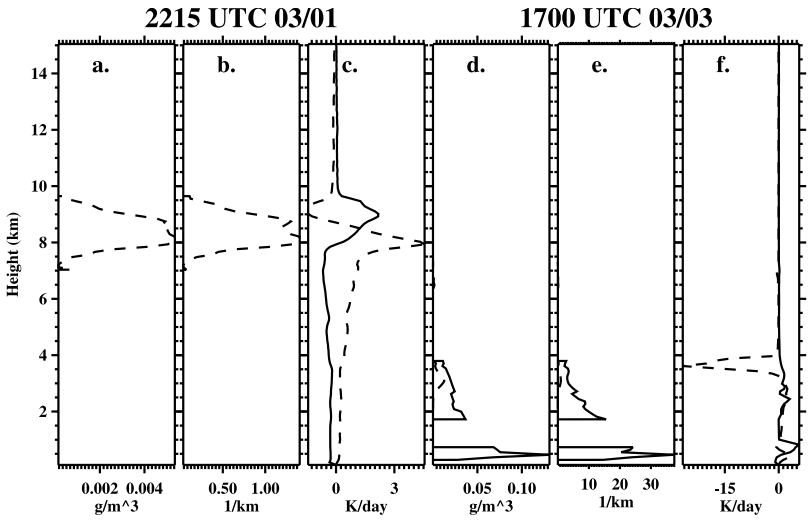

Figure 8. Illustration of the microphysical and radiative properties and the associated heating rates for two selected profiles during the 1–3 March case study denoted by the thin black lines drawn vertically through the height-time section of radar reflectivity in Figure 5. The profiles are from (a–c) 2215 UTC on 1 March and (d–f) 1700 UTC on 3 March. For each profile, the condensed liquid (solid lines) and ice water (dashed lines) profiles in units of g m^{-3}, the extinction profiles due to the liquid (solid lines) and ice (dashed lines) in units of m^{-1} and the resulting solar (solid lines) and IR (dashed lines) heating rates in units of K day^{-1} are depicted.

Mlawer et al. [1997] and the two-stream longwave fluxes are derived using 16 bands between 3.2 and 52 μm.

[21] Figure 8 shows two specific examples of the CPC results during the 1–3 March period. The heating rates that we show here are instantaneous values calculated from the 5-min averaged profiles expressed relative to the clear sky. In other words, we have subtracted the instantaneous clear sky heating rate from that diagnosed in the cloudy sky to show the cloud-induced heating. At 2215 UTC on 1 March, a pulse of cirrus was passing over the SCF in the southwesterly flow ahead of the advancing storm system. The layer at this time extended from 7.5 to 10 km and, using the retrieval algorithm described by *Mace et al.* [2002], the IWP of the layer was estimated to be 7.6 g m^{-2} with the IWC peaking in the middle of the layer. With an effective radius of 28 μm, the layer optical depth was estimated to be approximately 1.9 at this time. We diagnose weak solar heating in this layer that peaks near the middle of the layer at approximately 2 k day^{-1}. In the IR, we find cloud base heating of approximately 4 k day^{-1} changing to cloud top cooling on the order of 2 k day^{-1}. We discuss validation of the microphysical and radiative quantities below and the uncertainty of the derived heating rates in part 2.

[22] At 1700 UTC on 3 March, three cloud layers were observed by the MMCR. During this period, the lower stratocumulus layer was thinning with occasional breaks in the layer passing over the SCF. Above the boundary layer, a 2 km deep layer based near the freezing level passed overhead while cirrus, barely sensed by the MMCR, was observed in the upper troposphere. The total liquid water path at this time was retrieved from the MWR (Figure 3) and reported to be 86 g m^{-2}. Since both the boundary layer cloud and the middle level layer could potentially have had liquid water, the parameterization discussed earlier is used to distribute that water among these layers. The lower layer is attributed 40 g m^{-2} of liquid with the remainder assigned to the super cooled portion of the cloudy column. The lower layer had generally higher water contents but was just a few hundred meters thick at this time compared to the supercooled layer of more than 1 km depth. Because the determination of the liquid and ice water contents of layers in the mixed-phase temperature region are independent of one another, we find in this layer that the ice water path (8 g m^{-2}) derived from equation (1) is substantially smaller than the layer liquid water path. Note the extinction profile of the liquid is dominant with lower boundary layer cloud having an optical depth of 12 while the mixed phase layer had an optical depth of 13. The cirrus near 8 km is diagnosed to be quite tenuous with a water path from the *Liu and Illingworth* [2000] regression of approximately 0.5 g m^{-2} and optical depth near 0.1. The heating profile in this column is dominated by strong cloud top cooling of the mid level layer compensated somewhat by weak solar heating. Interestingly the cloud top of the boundary layer cloud does not cool substantially because of the presence of the optically thick layer above it although there does appear to be weak cloud base warming of the boundary layer cloud. The lack of cloud top cooling during this period is coincident with the thinning and partial dissipation of the stratocumulus. These changes to the cloud layer could have resulted through suppression of radiative destabilization of the cloudy boundary layer although there are certainly other reasonable explanations.

[23] In Figure 9, we show the cloud induced radiative heating for the storm system that passed over the SCF between 1 and 3 March. The largest convergence of radiative flux occurred near the cloud top region of the mixed phase and low clouds in the middle and lower troposphere. Solar heating in the optically thick portions of this region averaged 2–3 k day^{-1} while some solar

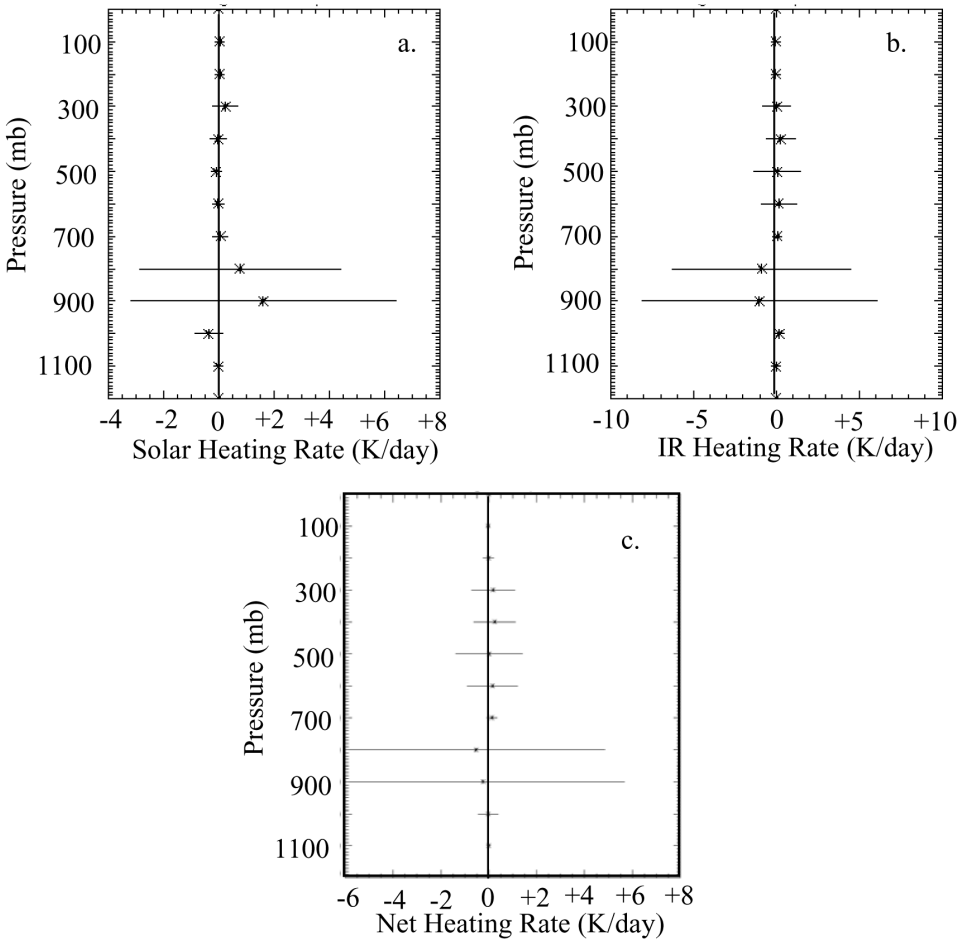

Figure 9. Mean and uncertainty of cloud-induced heating rate profiles collected in vertical pressure bins for the case study period from 1–3 March. The averaged values (depicted in units of K day^{-1}) are derived from instantaneous quantities calculated using 5-min averaged data. (a) Solar heating rates, (b) IR heating rates, and (c) net heating rate. Derivation of the uncertainties of these quantities is discussed in detail in part 2.

cooling is noted in the surface layer below the mean cloud base where the thicker clouds above attenuated solar radiation that would have been absorbed by water vapor in the boundary layer. The upper troposphere experienced primarily heating in both the solar and IR associated with the cirrus that occurred in advance of the storm system on 1 March. The time-averaged net heating profile for the 72 hour period shows cloud-induced cooling in the lower troposphere and heating aloft for a net atmospheric radiative effect of -7 W m^{-2} due primarily to the a net loss of IR energy. Overall the surface experienced 9 W m^{-2} of heating during this period (+14 W m^{-2} in the IR and -4 W m^{-2} in the solar) and the TOA experienced +3 W m^{-2} of heating (-5 W m^{-2} solar and +8 W m^{-2} in the IR). For completeness, we include error bars with these quantities derived using the validation statistics presented below and the technique outlined in part 2. Obviously, the uncertainties in the derived radiative effects are significant.

2.3. Validation of the Column Physical Characterization

[24] Our approach to characterizing the physical state of the atmospheric column using ground-based remote sensing data is unique since we merge many data sources through an ad hoc combination of parameterizations and retrievals linked together through various assumptions. Random and systematic error can enter the process at any point and this error has the potential to become amplified through the processing algorithms we employ. Therefore it is critical that the results are validated carefully with independent observations. Clearly, the most appropriate validation of this approach would come about by comparing the cloud microphysical properties with in situ aircraft data. This has been accomplished for the algorithms we apply to boundary layer clouds [*Dong and Mace*, 2003] and cirrus clouds [*Mace et al.*, 1998, 2001, 2002, 2005]. An independent aircraft data set to test the mixed phase retrievals requires in situ measurements of ice water content and particle size distributions in conjunction with ground-based Doppler radar and MWR observations. To our knowledge, an additional data set like that collected in March 2000 over the SGP does not exist although we do show a comparison of the ice phase regression parameterization in Figure 6 and Table 2. In lieu of more detailed in situ comparisons, we use comparisons with radiometric quantities measured and retrieved at the ground and the TOA. Since the derived

radiative properties of the clouds and their calculated effects on the radiation streams would accumulate errors, any significant problems with our analysis technique would become apparent in systematic biases and RMS differences compared to observations. We use retrievals of the cloud optical depth from multi filter rotating shadowband radiometers (MFRSR) as well as flux observations at the surface and the TOA for validation with the assumption that reasonably unbiased comparisons of the CPC results with these quantities is sufficient to establish the skill of the technique for the stated purpose of evaluating the radiative feedbacks of clouds.

[25] The cloud optical depth record that we use for validation is derived using the algorithm described by *Min and Harrison* [1996a] and *Min et al.* [2004]. *Min and Harrison* [1996a] developed a family of inversion methods to infer optical properties of clouds from diffuse measurements at the multifilter rotating shadowband radiometer (MFRSR) 415-nm channel, together with cloud liquid water path from MWR. The MFRSR allows accurate determination of atmospheric transmittances at 415, 500, 615, 673, 870, and 940 nm without requiring absolute calibration because it measures both total horizontal irradiance and direct-normal irradiance using the same detectors by a blocking technique. Consequently Langley regression of the direct-normal irradiance taken on stable clear days can be used to extrapolate the instrument's response to the top of atmosphere, and this calibration can then be applied to the total horizontal irradiance during overcast periods. Transmittances are calculated subsequently under cloudy conditions as the ratio of the uncalibrated MFRSR signal to the extrapolated top-of-atmosphere value. The cloud optical depth and cloud drop effective radius are simultaneously retrieved through the use of a nonlinear least squares minimization in conjunction with an adjoint method of radiative transfer [*Min and Harrison*, 1996b]. *Min et al.* [2004a] take advantage of simultaneous spectral measurements of direct and diffuse transmittance of an MFRSR and temporal variations to retrieve optical depths for optically thin clouds from direct beam irradiances. To minimize the interference of gaseous absorption, the retrieval algorithm selects the 415 and 860-nm channels, and separates aerosols from thin clouds on the basis of their temporal and spectral characteristics. The thin cloud algorithm provides accurate retrievals of optical depth for clouds with visible optical depth <5. Various comparisons and validations for the narrow band retrieval algorithm of *Min and Harrison* [1996a] have been reported [*Min and Harrison*, 1998; *Barnard et al.*, 2001; *Min et al.*, 2003]. An uncertainty analysis of thin cloud retrievals has been conducted and shows that it produces retrievals that are better than 5% or 0.05 when cloud optical depth is less than 1 [*Min et al.*, 2004].

[26] The optical depth comparison for the case study period is shown in Figure 10 (note that no MFRSR observations are available on 2 March). For optical depths less than 5, we are especially sensitive to horizontal variations in cloud structure due to the use of direct solar beam transmittance in the MFRSR optical depth retrieval. While the overall comparison on this day is reasonable, the trend observed by the radar retrievals is not identical to the MFRSR retrievals during the middle portion of the day when, according to Figure 5, the cirrus layer thinned considerably in the vertical column directly above the radar. However, the overall comparison of the instantaneous optical depth values of this cirrus event appears reasonable. On 3 March, the clouds observed at SGP, range from optically and physically thin stratocumulus to optically thick multilevel clouds (Figure 5). The CPC and the MFRSR retrievals (Figure 10b) capture this variability in the optical depth time series with good agreement. In order to perform a more rigorous comparison, we examine the months from February through December 2000. To minimize sensitivity to horizontal variations in cloudiness that might influence the hemispheric spectral flux measurements we average the CPC and MFRSR observations for 30 min and exclude any periods with less than 80% cloud occurrence as derived from the MMCR data averaged over this 30-min interval. In the optical depth range less than 5, we also restrict the time period to the hours surrounding local solar noon (1700–2100 UTC). Recall also, that the CPC is not reliable during precipitation and therefore these periods are excluded. The comparison shown in Figure 11 is summarized in Table 3. The high optical depth events include warm liquid phase layers like on 3 March but also deep and mixed phase cloud layers where the cloud microphysical properties are derived with the mixed phase cloud parameterization scheme. The optical depth comparison is encouraging because it lends some degree of credence to our characterization of the cloud microphysical properties.

[27] In order to examine the radiative heating of the atmosphere due to clouds, we must also consider to what degree of precision the solar and IR radiative fluxes at the surface and TOA can be characterized. The TOA flux values are not direct measurements but are derived from half-hourly GOES 8 data using a set of narrow- to broadband conversion algorithms. These algorithms are of the same form and derived in the same manner as those reported by *Minnis and Smith* [1998]. However, they are based on correlations between 1998 GOES 8 visible (0.65 μm) and infrared (10.8 μm) radiances and their respective shortwave (SW; 0.2–5 μm) and longwave (LW; 5–100 μm) flux counterparts from the Clouds and Earth's Radiant Energy System (CERES) scanner [*Wielicki et al.*, 1998] on the Tropical Rainfall Measuring Mission (TRMM) satellite. The RMS errors in SW albedo and outgoing LW radiation (OLR) regression fits to the TRMM data are 0.021 and 7.2 W m^{-2}, respectively, or 8.3 and 2.8%. The regression formulae were applied to the 2000 GOES 8 data calibrated using the TRMM Visible Infrared Scanner as in the work by *Minnis et al.* [2002].

[28] Additionally, the GOES data are used to derive cloud amount, altitude, temperature, and visible optical depth using the Layer Bispectral Threshold Method (LBTM), which was applied to hourly GOES 8 data taken between 1995 and 2003 over a 10° latitude by 14° longitude domain centered on the SCF [*Minnis et al.*, 1995; *Khaiyer et al.*, 2002]. The LBTM uses the RUC temperature and humidity profiles to account for atmospheric attenuation of the visible and infrared radiances and a set of fixed ice and water cloud models to derive optical depth from the reflected radiance fields [*Minnis et al.*, 1993]. Both the cloud properties and

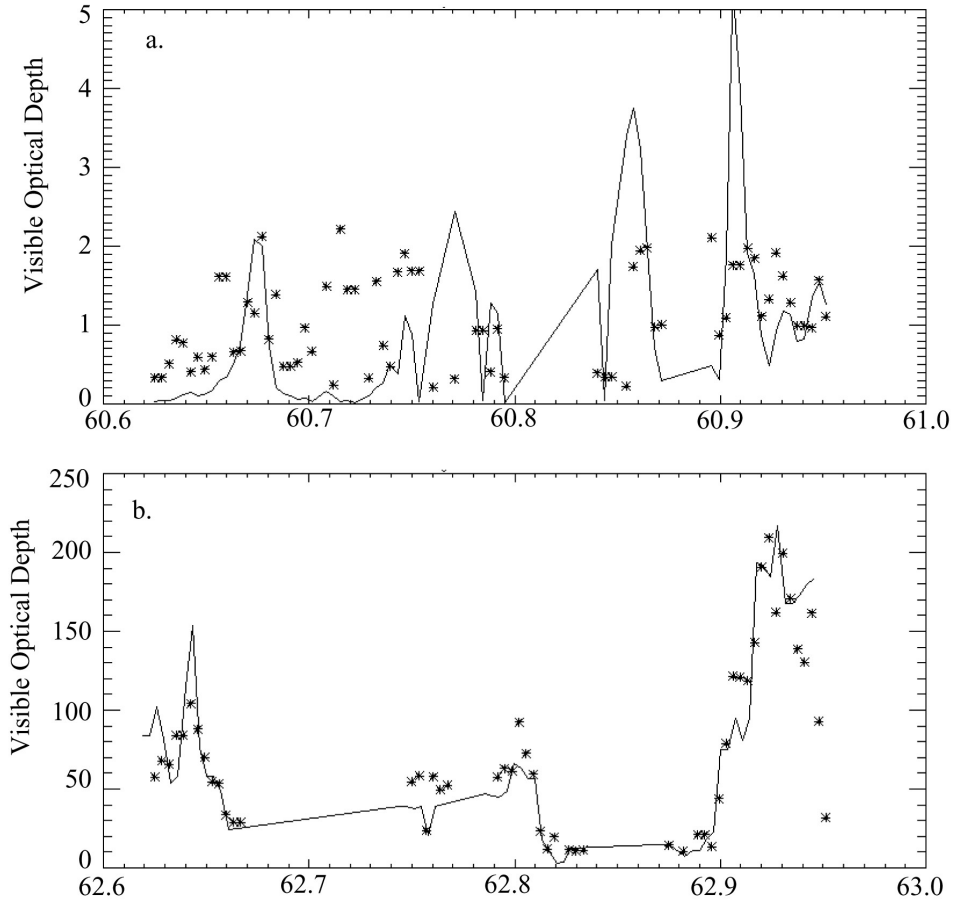

Figure 10. Comparison of total optical depth derived from the MFRSR (asterisk) and calculated (solid line) using the CPC technique for (a) 1 March and (b) 3 March. Time is shown in Julian day.

TOA fluxes are averages for a 0.3° region centered on the SCF.

[29] At the surface, ARM deploys a suite of well-calibrated up and down looking solar and IR broadband radiometers, and these data streams are used here, averaged to the 5-min time resolution of the CPC, for comparison. In an effort to effectively characterize the effects of clouds on the solar flux, we combine the observed downwelling solar flux with estimates of the clear sky solar flux derived using the procedure described by *Long and Ackerman* [2000]. Use of this quantity allows us to estimate the effects of clouds on the solar flux and to examine the fractional change in downwelling solar flux due to clouds. Similar quantities can then be calculated from the CPC diagnostic using the cloudy sky and clear sky solar flux calculations. Since no similar estimate of the downwelling clear sky IR flux has been devised, we examine just the cloudy sky downwelling and net surface longwave flux instead of the surface longwave cloud effect.

[30] When performing the radiation calculations we assume that each column is independent and plane parallel and that the observed vertical distributions of clouds during the 5-min averaging period correspond to layers that are overcast. As an example, we complete our description of the 1–3 March case study by comparing the calculated fluxes to

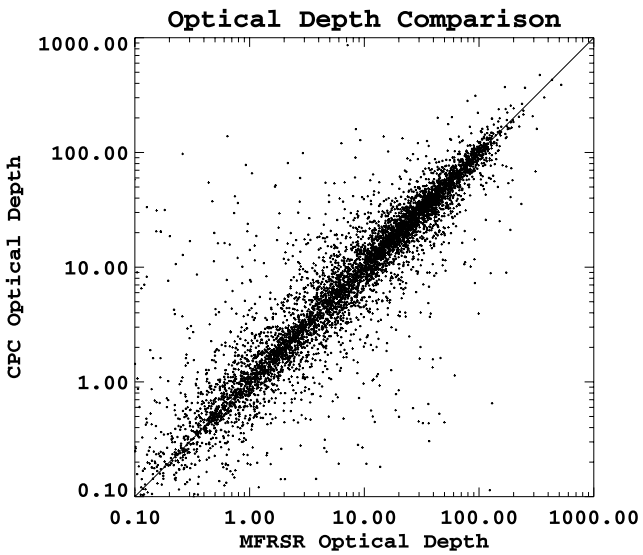

Figure 11. CPC optical depth compared to MFRSR optical depth for the period from March to December 2000. Only the period between 1700 UTC and 2100 UTC was considered for MFRSR optical depth less than 5.

Table 3. Summary of the Optical Depth Comparison Between the MFRSR Value and CPC Derived Values for the Year 2000[a]

Fractional Bias	Median Fractional Error	Slope of Linear Fit	Intercept of Linear Fit	Correlation Coefficient	Normal Deviation	Number of Obs
0.004	0.18	0.63	8.0	0.59	32	6576
0.006	0.09	0.89	0.08	0.89	0.39	6576

[a]The second row is the same as the first except referenced to the $\log_{10}$ of the optical depths.

observed TOA and surface fluxes in Figure 12. The time series comparisons suggest reasonable agreement in all quantities with some notable exceptions. On 1 March, the cirrus increase the TOA albedo from approximately 20% to as high as 45% late in the day when the layer thickened and the zenith angles increased. The calculations track the GOES-derived albedos quite well while at the surface the variability in the downwelling solar also suggests reasonable agreement. A notable bias is discernable in the surface solar downwelling fluxes. This is due, at least partially, to the fact that our calculations do not include aerosol – an omission that would cause only small biases when considering the cloud-induced radiative perturbations. The OLR values on 1 March show significant offsets during much of the day and only come into agreement after about 2100 UTC when the clouds thicken. At the surface, a persistent 5–10 W m^{-2} bias seen between the thick cloud events may be due to thicker clouds that are not observed by the vertically pointing MMCR at that time. However, the peaks in emission that correspond to the periods when the thicker portions of cirrus are overhead show good agreement. During the remainder of the period, we find that the albedo agrees well although the variability observed by the satellite is much less than derived instantaneously from the surface data. This difference in variability is due to the smoothing effect of averaging over a larger area in the GOES data. The OLR continues to show occasional biases particularly on 3 March suggesting perhaps that thin cirrus that was not observed by the MMCR resulted in a 10–15 W m^{-2} high bias in the calculations. Overall, the surface solar flux agrees very well in the heavy overcast periods while the downwelling IR shows a persistent 5 W m^{-2} bias through 2 and 3 March for which we have not been able to determine a cause. With respect to the profiles we considered in Figure 8, Table 4 summarizes the flux comparisons.

[31] While case studies are useful, a long-term comparison of fluxes allows for a more rigorous characterization of the CPC errors. The objective of this initial study is not to consider partly cloudy skies or periods where the cloud properties are rapidly changing. While we recognize the importance of such situations, it is more instructive to minimize this source of variability so that the validity of

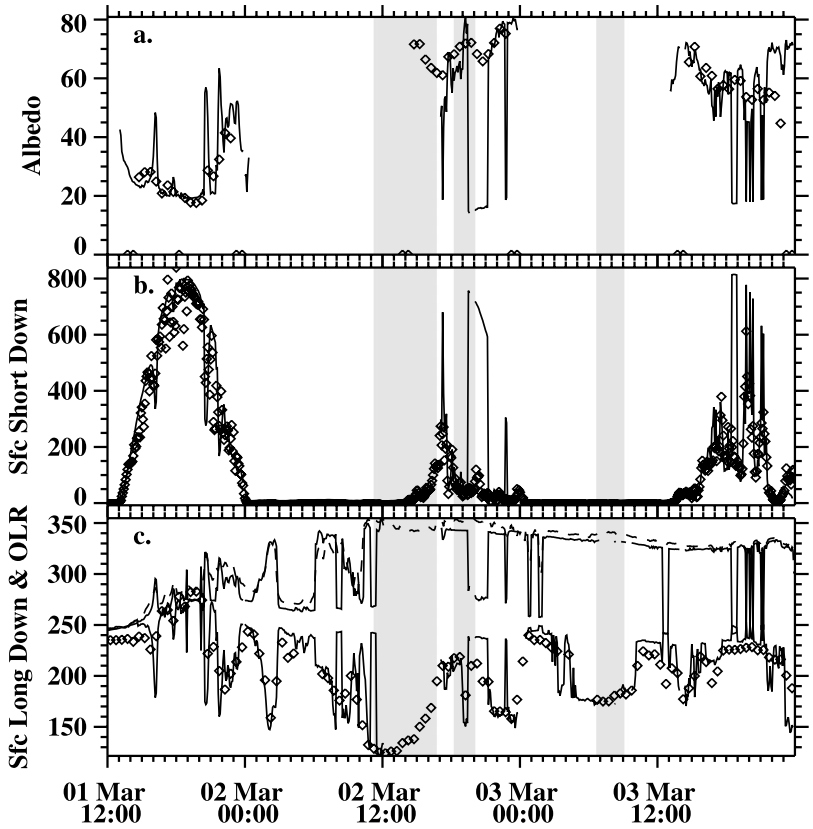

Figure 12. Comparison of derived fluxes (solid lines) with observations. (a) Calculated albedo compared with values derived from GOES. (b) Surface solar flux (W m^{-2}) compared with derived values and (c) OLR (lower values) and the surface downwelling longwave (higher values) (W m^{-2}).

Table 4. Comparison of Calculated to Observed Fluxes (Observations Are in Brackets) at the Times Shown in Figure 8[a]

Time	TOA Albedo	TOA OLR, W m^{-2}	Sfc IR Down, W m^{-2}	Sfc Solar Down, W m^{-2}
2215 UTC 1 March	0.41 [0.41]	210 [187]	293 [309]	295 [251]
1700 UTC 3 March	0.51 [0.56]]	215 [205]	324 [327]	295 [200]

[a]With the exception of albedo, the units are W m^{-2}. The first number in each cell is the calculated value.

the cloud properties can be discerned. Therefore we consider only situations that meet specific criteria during 30-min averaging periods centered on the GOES observation times. We define the vertical cloud occurrence fraction during this period as the fraction of original 36-s MMCR columns that have cloudiness reported at some level. Since the GOES algorithm also estimates a pixel level cloud amount, cloud base, and cloud top, we additionally require the satellite pixel(s) nearest the SCF to have a similar cloud cover and to be of a similar type. For the purpose of this comparison, middle level clouds are defined to have bases greater than 3000 m and tops less that 6500 m. High clouds are defined as layer with bases above 6500 m while low clouds have tops below 3000 m. We define clear as a cloud occurrence fraction of 0 during a particular time period while broken clouds are assumed to have an occurrence fraction greater than 0.5 but less than 0.9. A period with scattered cloud cover has occurrence fraction greater than zero but less than or equal to 0.5 while overcast has occurrence fraction greater than or equal to 0.9. For comparison of the TOA and surface in a 30-min period, we require the cloud coverage to be of the same class (scattered, broken, or overcast). Also, the cloud type of the highest layer observed by the MMCR must be the same as the highest cloud type derived from the GOES data. With these constraints and definitions, we are able to reasonably evaluate the CPC, although, in order to acquire sufficient data to make the comparisons, we are forced to examine a long time period.

[32] Using data collected at the SCF during the year 2000, we compare several key quantities in Figure 13 for overcast cloud scenes and summarize the comparisons along with broken cloud scenes in Tables 5a and 5b where we show several quantities. At the TOA we include the upwelling IR flux ($L\uparrow_t$; W m^{-2}), the upwelling solar flux ($S\uparrow_t$; W m^{-2}), and the solar cloud effect ($CFC - NS_t$; W m^{-2}) defined as the difference in the net solar flux in cloudy skies from the net solar flux in clear skies where downward fluxes are considered positive. At the surface we show the downwelling IR flux ($L\downarrow_s$; W m^{-2}) and the surface solar cloud effect ($CFC - NS_s$). Since we are not attempting to model the effects of aerosol on the solar flux, at the surface we compare the fraction of the downwelling clear sky flux that has been removed by cloud ($S\_Frac\downarrow_s$) where the clear sky surface solar flux observations are derived from the technique described by *Long and Ackerman* [2000]. At the TOA, the $CFC - NS_t$ observations use clear sky values derived from nearby pixels deemed to be clear. We do not attempt to show longwave cloud effect (CFC - NL) at either the surface or TOA. At the surface no clear sky equivalent derivations of upwelling or downwelling longwave fluxes are available, and at the TOA, the clear sky flux derived from nearby clear scenes will have a very different surface temperature and perhaps a different moisture profile than what is observed at the SCF. It is therefore impossible to compare the calculated longwave cloud effects with the observations.

[33] Overall, the comparisons shown in Figure 13 and Tables 5a and 5b are reasonable although we find significant scatter and some biases in several of the quantities. The solar radiation fluxes at the surface and TOA are, of course, very sensitive to the horizontal structure of the cloud field and the representativeness of the 30-min averaged CPC vertical profiles. It is encouraging to note that $S\_Frac\downarrow_s$ is essentially unbiased in the overcast scenes and that the scatter as measured by the median error and the normal deviation both decrease significantly in overcast scenes compared to broken scenes. These statistics are similar to those presented in a radiation closure study [*Mace et al.*, 2001] using cirrus cloud retrievals. The negative bias in $CFC - NS_t$ that is evident in Figure 13a is expected because the upwelling flux observed by GOES in nearby cloud-free pixels includes an aerosol contribution that would tend to reduce the observed cloud effect relative to an aerosol-free calculation. The bias evident in Figure 13c in $CFC - NS_s$ is not really represented in the -1% bias noted in Tables 5a and 5b because of compensating errors at lower optical depths. The bias at higher values of $S\_Frac\downarrow_s$ is consistent with aerosol reducing the net effect of clouds in the observations relative to what would be calculated assuming no aerosol although the magnitude of the offset shown in Figure 5c is larger than we would expect from aerosol.

[34] Compared to the exhaustive validation presented by *Rossow and Zhang* [1995], our results suggest validity at least comparable to their ground-based comparisons although, as expected, we have significantly more scatter in our TOA comparisons. This is not surprising given the technique used in satellite retrieval studies where irradiances from broadband radiometers such as ERBE are used to validate a product derived from narrow band radiances and reflectances where the properties of the atmospheric profile, including the clouds, serve essentially as transfer functions to convert between the narrowband measurements and the broadband fluxes. Highly correlated and unbiased comparisons would be expected in such circumstances. With the exception of the Z-R cirrus retrieval algorithm, we do not use radiances or irradiances in the retrievals and, validation with radiation measurements at the surface and TOA is reasonable. On the basis of our comparisons with MFRSR optical depths where nearly unbiased agreement was found relative to the factor of 1000 variation in the quantity, and on the basis of small biases in the TOA and surface flux quantities, we conclude that the CPC technique applied to ARM data can reasonably characterize the macroscale properties of clouds as well as the gross effects that the clouds impose on the solar and infrared radiation streams.

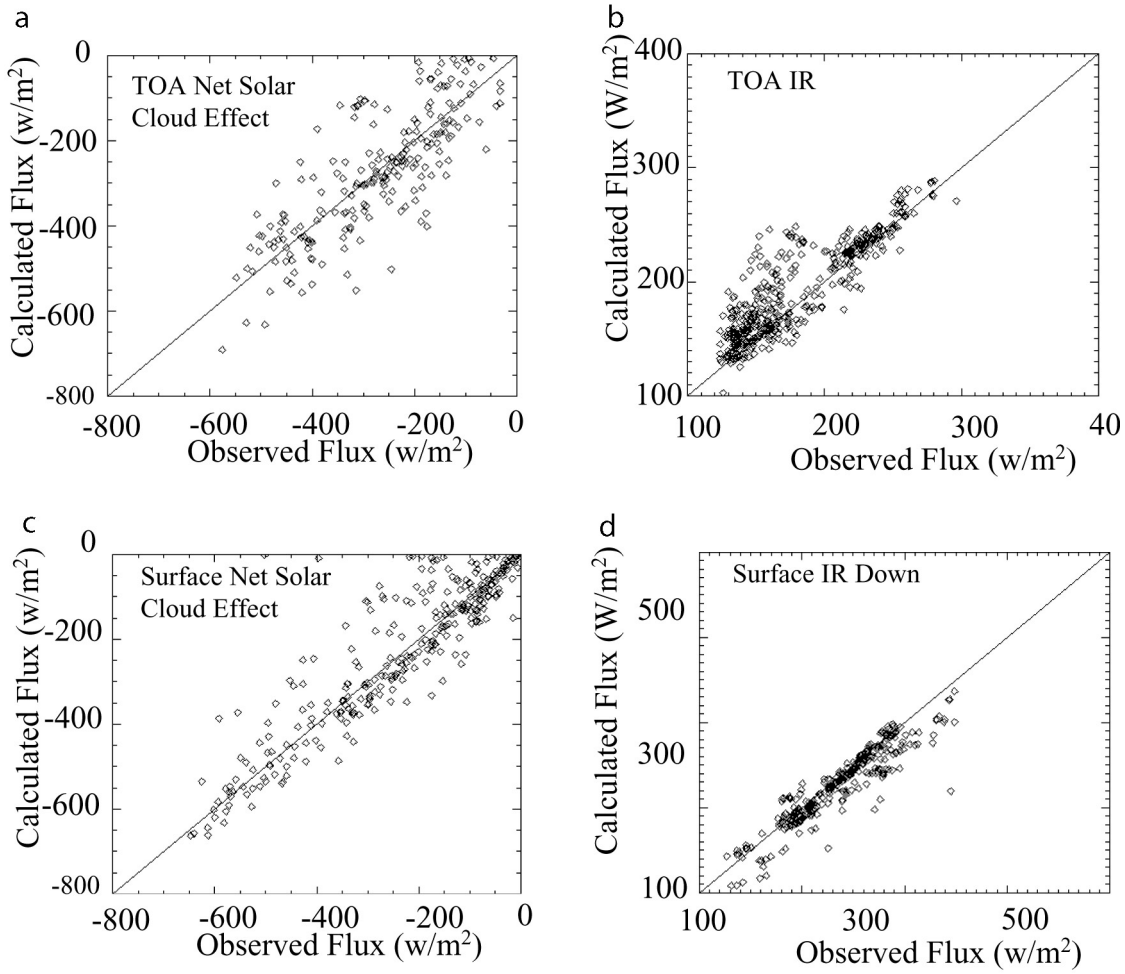

Figure 13. Comparison of (a and b) TOA and (c and d) surface cloudy fluxes with CPC calculations for all overcast scenes during the year 2000.

The quantitative uncertainty in the cloud radiative effect and cloud radiative forcing is discussed in detail in part 2.

3. ISCCP and LBTM Comparison

[35] The climatology of CTP and τ_{tot} such as those produced by ISCCP and by ARM using the LBTM [*Minnis et al.*, 1995; *Khaiyer et al.*, 2002] are becoming standards against which many models are being evaluated. *Zhang et al.* [2005], for instance, found that of the 10 GCMs they examined, all significantly underpredicted the global occurrence of middle level clouds and significantly overestimated optical thickness relative to satellite-derived results. Because such conclusions have far-reaching implications for model development and interpretation, we compare the CTP and total column optical depths (τ_{tot}) derived from the ARM

Table 5a. Comparison Statistics of TOA and Surface Radiation Quantities Calculated Using the CPC Technique With Observations[a]

	Median Fractional Difference	Fractional Offset	Correlation Coefficient	RMS Diff	Slope of Linear Fit	Intercept of Linear Fit	Mean Obs	Normal Deviation	Number of Obs
TOA									
$S\uparrow_t$	0.16	−0.05	0.72	75	0.81	55	381	113	657
$L\uparrow_t$	0.05	+0.03	0.86	16	0.81	46	204	21 23	993
$CFC - NS_t$	0.31	+0.01	0.77	99	0.86	−36	−226	97	527
SFC									
$S\_Frac\downarrow_s$	0.24	−0.06	0.73	0.22	0.88	0.0	0.52	0.21	709
$L\downarrow_s$	0.03	−0.03	0.89	15.	0.85	38	337	20	762
$CFC - NS$	0.27	+0.12	0.69	152	0.66	−66	−236	125	681

[a]At the surface we compare with ARM pyranometer and pyrgeometer measurements and at the TOA we compare with broadband fluxes derived from GOES radiances using the LBTM algorithm. The surface and CPC averaging time is 30 min. Period covered is the entire year 2000. All fractional values are reported relative to the mean of the observations. Units of all nonfractional values are W m^{-2}. All broken and overcast nonprecipitating cloud scenes are included. See the text for definition of symbols.

Table 5b. As in Table 5a Except Only Overcast Scenes Are Included

	Median Fractional Difference	Fractional Offset	Correlation Coefficient	RMS Diff	Slope of Linear Fit	Intercept of Linear Fit	Mean Obs	Normal Deviation	Number of Obs
TOA									
$S\uparrow_t$	0.10	−0.02	0.84	63	1.02	−19	414	90	256
$L\uparrow_t$	0.06	+0.06	0.88	14	0.86	37	180	19	419
$CFC - NS_t$	0.19	−0.01	0.80	88	0.92	−24	−274	88	209
SFC									
$S\_Frac\downarrow_s$	0.14	−0.05	0.78	0.17	0.97	0.01	0.61	0.17	292
$L\downarrow_s$	0.02	−0.02	0.93	11	0.87	36	336	16	323
$CFC - NS$	0.17	+0.03	0.90	78	0.93	−9.5	−243	77	287

data analysis to similar quantities derived from the ISCCP [*Rossow and Schiffer*, 1991, 1999] and by the LBTM algorithm. Both satellite algorithms use visible and thermal infrared measurements from available weather satellites, combined with meteorological analyses, to derive physical descriptions of the atmospheric column very much like we are creating with ground-based data from the SCFs except that the satellite results are global and extend over many years (decades in the case of ISCCP). While RZ95 and others have evaluated ISCCP using TOA and some ground-based radiation measurements with reasonable results, a statistical comparison of these satellite results with long-term ground-based measurements of cloud top pressure and derived optical depth has not been reported.

[36] The ISCCP algorithm samples the geostationary pixel-scale satellite data in 3-hourly intervals and at 30 km horizontal spacing. Therefore, to build up reasonable statistics for the comparison of ISCCP to ARM data, we derive the mean and standard deviation of the ISCCP values in 100 km and 250 km domains that are centered on the ARM SCF. The LBTM retrievals are calculated and recorded for every available image at the pixel scale. We have examined statistics from the pixel nearest the ARM SCF and statistics derived from the 8 surrounding 0.3° regions with similar results. Figure 14 shows the frequency of occurrence histograms of joint CTP and τ_{tot} for March 2000 as reported by ISCCP, LBTM, and derived from the ARM data along with results from an algorithm that has been developed (ICARUS [*Webb et al.*, 2001]) to take predicted, or in our case diagnosed, cloud property profiles and convert them into radiance and reflectance that would be observed by the satellite radiometers and then mimic the ISCCP CTP retrieval. A major part of the ICARUS algorithm as applied to model output is to account for the spatial cloud fraction and overlap. Here, since we are dealing with point measurements, we only derive the ISCCP-estimated CTP with the ICARUS algorithm.

[37] In Figure 14, both similarities and differences can be seen. The two satellite algorithms appear similar in the upper troposphere except that ISCCP places much of the optically thin cirrus into the upper left bin. Both algorithms show a minimum of occurrence in high clouds of medium optical thickness. Both satellite algorithms also diagnose maxima in middle and lower-tropospheric optically thick clouds and find deep optically thick clouds near 400 mb. LBTM diagnoses more lower-tropospheric optically thin clouds than does ISCCP. The ARM data show similar peaks in occurrence of optically thick lower-tropospheric clouds although the optical depths are somewhat higher and more optically thick low clouds are found. In the upper troposphere, thin cirrus predominates and more clouds of medium optical thickness are found compared to the satellite algorithm results. The most obvious differences exist in the lower-tropospheric and midtropospheric clouds of medium optical thickness which the ISCCP and LBTM find more frequently than either ARM or the ICARUS simulation. The ICARUS results do tend to increase the frequencies in this region although not to the extent diagnosed by the ISCCP or LBTM algorithms.

[38] To better understand the differences in the histograms, it is instructive to compare the actual time series of CTP and τ_{tot}. For reference, we show the diagnosed condensed water height-time section for March 2000 in Figure 15a. The CTP and τ_{tot} time series are in Figures 15b and 15c where we plot the hourly averaged quantities derived from the ARM data for clarity; the 5-min data show more variability that obscures important details. From a broad perspective, the comparison is encouraging with ISCCP and LBTM reasonably capturing the variability in the evolving cloud structures over the SGP region during this month as compared to the ARM diagnostics. A closer examination reveals the sources of the differences noted in Figure 14.

[39] Between the two satellite algorithms we find that the primary source of the differences in Figure 14 is from the CTP quantity. The optical depths derived by ISCCP and LBTM are similar through the month. With respect to CTP, thin cirrus events show the largest discrepancies between the satellite algorithms and observations. ISCCP has a tendency to place these optically thin clouds into a default pressure bin at 100 mb while LBTM often diagnoses these clouds in the middle and lower troposphere (i.e., 2, 9, and 28 March). The best example of this is on 1 March when LBTM places much of the thin cirrus between 700 and 800 mb. Other discrepancies are evident such as on 18 March when ISCCP places the thick midlevel and low-level overcast cloud well into the boundary layer while LBTM reports clouds more in the middle troposphere above the measured cloud tops. With the exception of thin cirrus in ISCCP, we find that the satellite algorithms nearly always bias CTP to higher pressures (lower in physical height) than the measurements when they are biased. This seems to occur especially in multi layer situations when cirrus occur above thick midlevel and low-level clouds (i.e., 3, 7, and 16 March) and occasionally in thick cirrus/altostratus (i.e., 13 March). When thin cirrus are present over midlevel and low-level clouds, the satellite algorithms place clouds somewhere between these two cloud layers. Curiously, this bias into the middle troposphere also occurs in low clouds on 30 March although there may have been higher clouds in

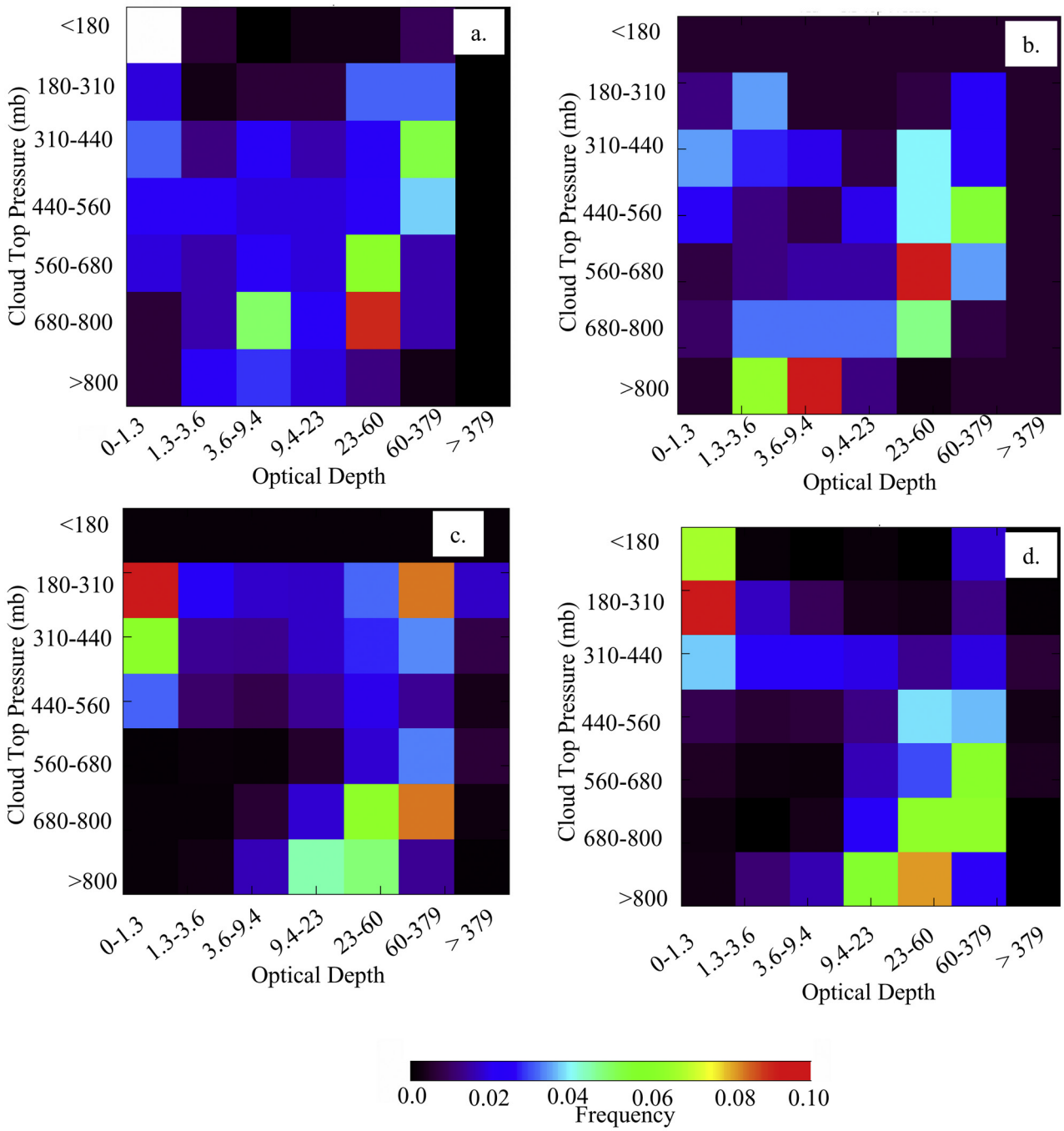

Figure 14. Cloud top pressure and total visible optical depth histograms from (a) ISCCP in a 250 km domain centered on the SGP site, (b) the nearest pixel of the LBTM algorithm to the ARM SGP site, (c) the ARM data CPC diagnostic, and (d) the ICARUS simulation of the ISCCP algorithm using the ARM CPC information as input. The period covered is March 2000 during daylight hours.

the area not yet over the SCF. With the exception of the possibility of being biased to lower heights because of tenuous cloud tops that are below the detection threshold of the MMCR and attenuation in heavy precipitation clouds, the CTP from the ARM data is an observation while the satellite-derived CTP is more of a derived quantity; especially in clouds with τ_{tot} less than about 5 where the clouds are partially transmissive and the radiating center of the cloud is not close to cloud top.

[40] For τ_{tot} we find that the ARM CPC diagnostic correlates well with ISCCP and LBTM. We find reasonable agreement in the optically thinner cirrus clouds such as on 1, 6, 9, 21, and 31 March. Clouds of medium optical thickness also show reasonable agreement such as on 10 March, and 13 March. When ISCCP and LBTM disagree with the ARM diagnostic in the thin and medium optically thick clouds the optical depth bias tends to be low. An example of this is on 2 March and 3 March which we

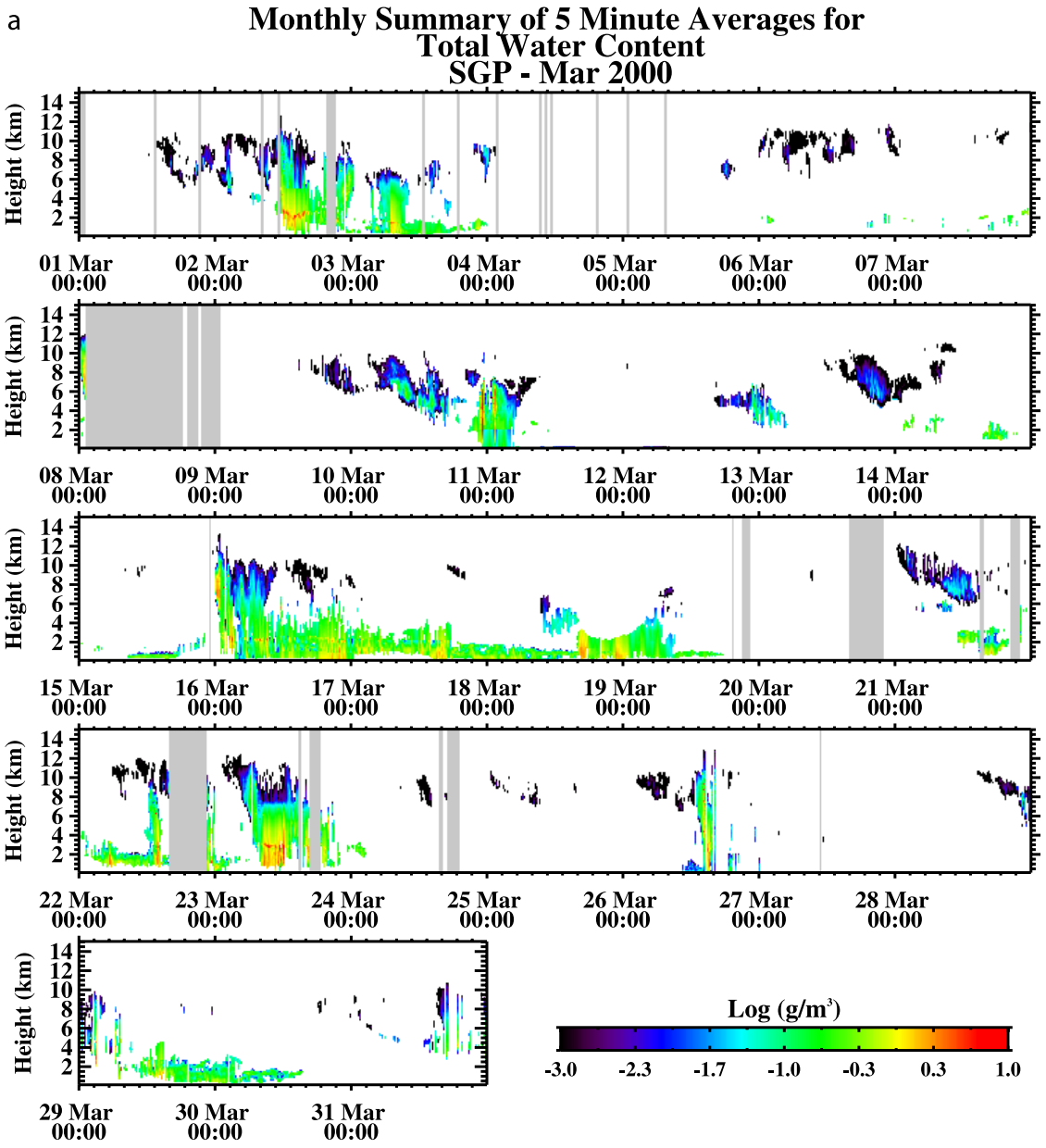

Figure 15. Time series of (a) total condensed water content diagnosed using the CPC technique during March 2000. (b) Comparison of cloud top pressure as derived from the ISCCP and LBTM satellite products with CPC-derived quantities. The ISCCP quantities are shown as means and standard deviations in geographic domains centered on the ARM SGP site. (c) As in Figure 15b except that total cloud optical depth is shown.

examined earlier in the case study analysis. Overall, the satellite algorithms are 30–50% lower than the values diagnosed with the ARM data on these days. The ARM τ_{tot} is generally higher than the satellite algorithms in very thick clouds like those that persisted from 15 to 19 March. The ISCCP and LBTM use reflectance models that maximize at optical depths of 256 and 128, respectively, because the reflectance field changes very slowly with increasing optical depths above 128. The difference in the reflectance for clouds with optical depths of 128 and 256 is within the uncertainty of most satellite visible channel calibrations. We note that only rarely is the ISCCP τ_{tot} greater than the ARM τ_{tot} such as on 22 and 23 March.

[41] Given just three observations per day for ISCCP and only daylight data from LBTM, a single month is not sufficient for quantitative comparison. We attempt a more rigorous comparison of CTP and τ_{tot} by examining data from the year 2000. For a comparison between the satellite algorithms and the ground-based instruments to be counted in the statistics shown in Table 6 and Figure 16, we require each of the 34 ISCCP pixels in the 250 km domain to be cloudy at the comparison time. Hourly averaged results from the CPC algorithm are compared to the LBTM and ISCCP results. We find that the ICARUS simulation of the ISCCP retrieval improves the CTP comparison. Even though the ICARUS result is strictly only defined for the

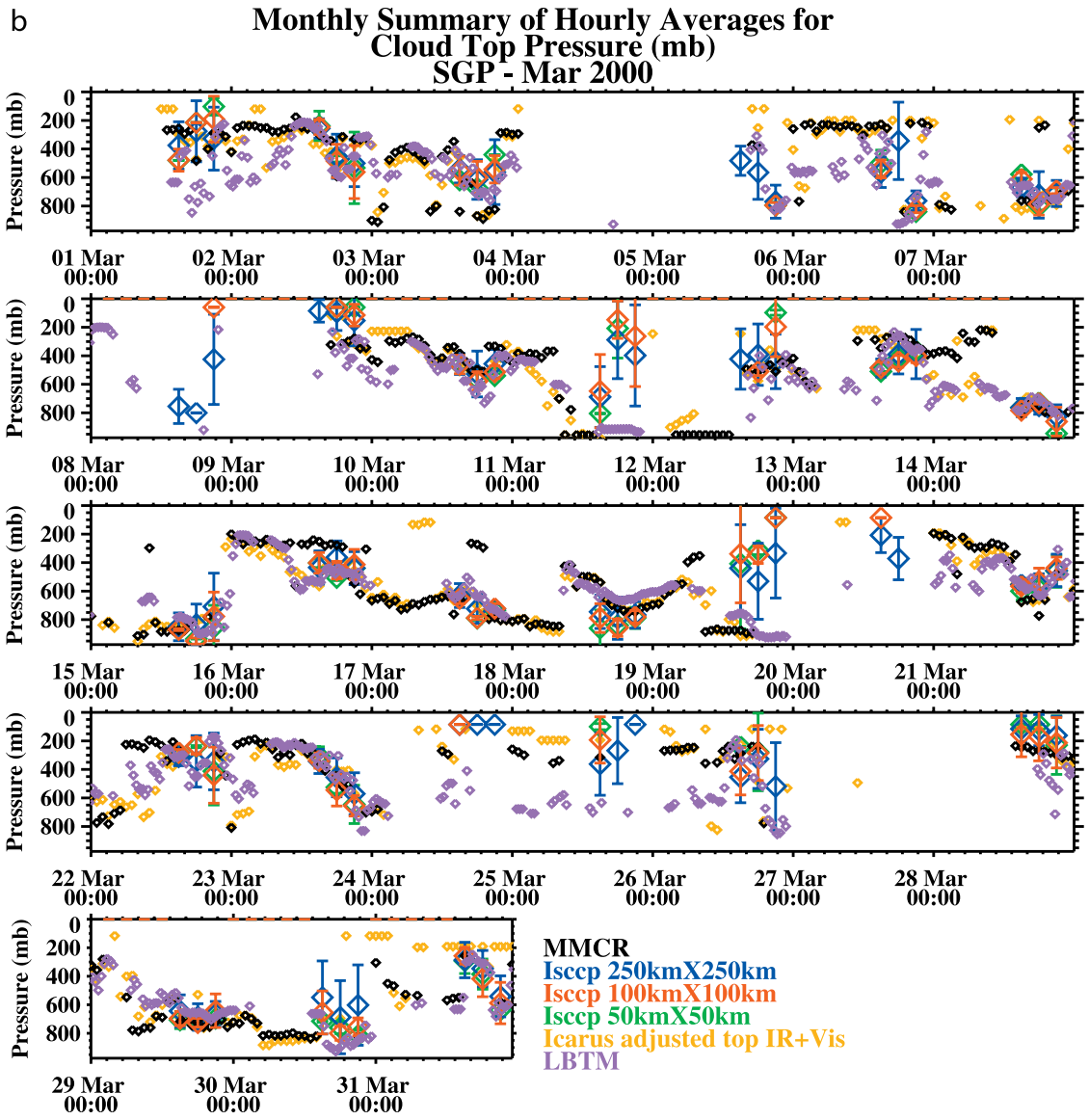

Figure 15. (continued)

ISCCP retrieval, we also compare it with the LBTM retrievals with similarly improved results. Table 6 shows that the correlation, the linear regression, and the normal deviation tend to improve for the simulation of the satellite algorithms. The only apparent drawback is the tendency for the ICARUS simulation to induce a slight negative bias in the comparisons. For τ_{tot} we find a reasonably strong correlation between the ground based results and the satellite algorithms like during March 2000 with the best comparisons occurring in the optical depth range from about 1 to 50. However, a negative offset seems to exist in the comparison at higher optical depths with a bias on the order of 4 db.

4. Summary and Conclusions

[42] We use continuous ground-based data collected at the ARM SCF to characterize the physical properties of the atmospheric columns including cloud occurrence, microphysical and radiative properties, and radiative fluxes. Objective algorithms presently exist to derive the microphysical properties of certain classes of clouds from millimeter radar data combined with other data sources. Several of those algorithms are employed in this work. There are, however, significant gaps in our ability to objectively retrieve cloud properties in the presence of deep and mixed phased clouds. The essential difficulties reduce to identifying what fraction of the liquid water path in such situations is due to clouds that exist at temperatures above freezing and what fraction of the total water path exists at supercooled temperatures. Beyond this, algorithms for identifying the condensed water contents, both ice and liquid, in supercooled clouds are presently not well established. Therefore we employ a simple parameterization of condensed liquid water content [*Kiehl et al.*, 1998] that produces a normalized distribution function with which we estimate the fraction of the observed liquid water path that is warm and supercooled. To the warm cloud layers, we apply published cloud property retrieval algorithms and to the cold liquid component, we use the distribution function

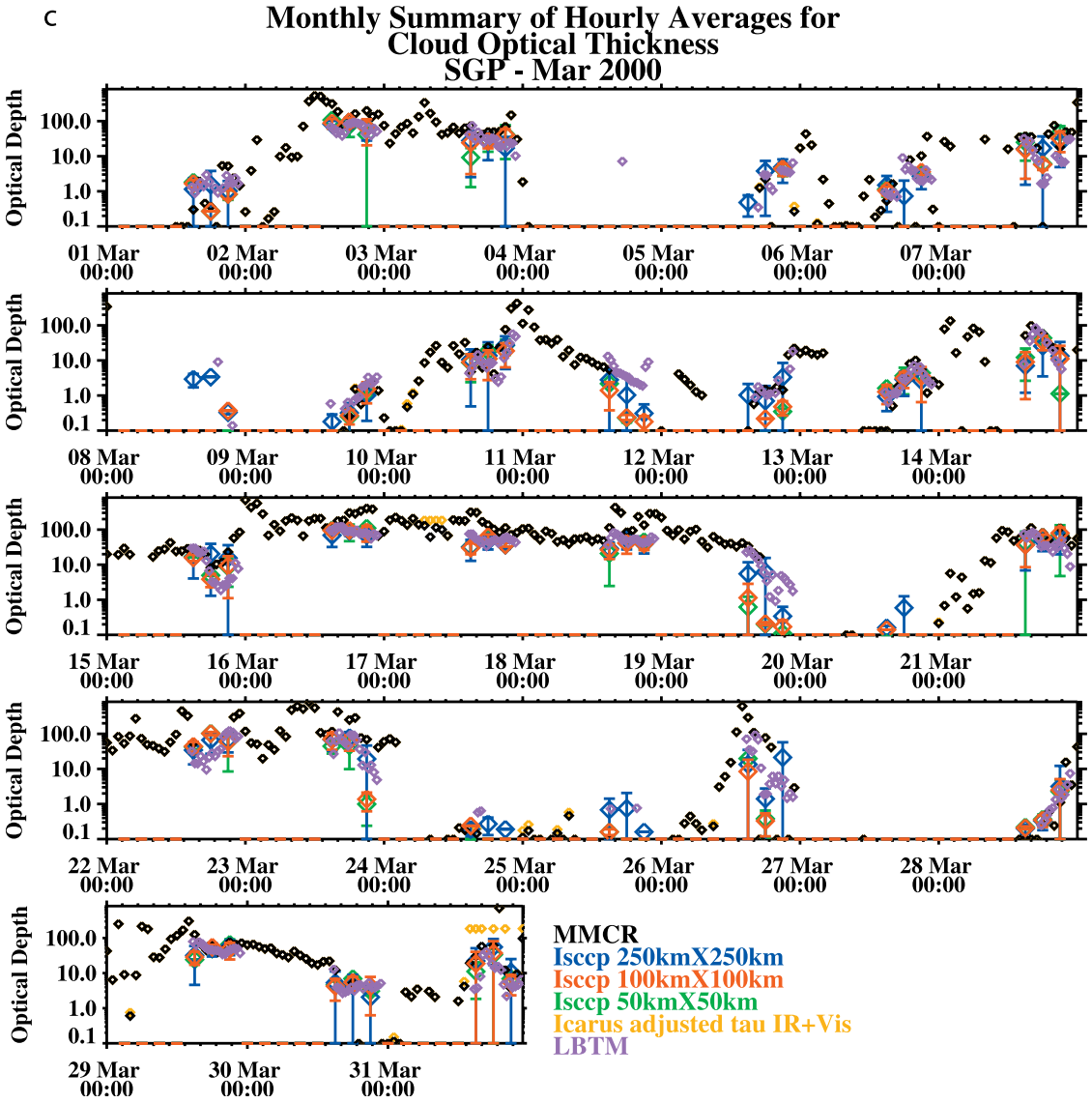

Figure 15. (continued)

Table 6. Statistics of the Comparison Between ARM CPC CTP and Tau With Results From LBTM and ISCCP[a]

Comparison	Median Fractional Error	Bias	Slope of Linear Fit	Intercept of Linear Fit	Linear Correlation	Mean ARM	Mean ISCCP/LBTM	Normal Deviation
CTP (CPC-ISCCP 250 km)	0.10	15	0.70	131	0.91	468	496	84
CTP (ICARUS-ISCCP 250 km)	0.12	39	0.78	71	0.92	456	496	68
CTP (CPC-ISCCP 100 km)	0.13	15	0.8	83	0.92	472	487	58
CTP (ICARUS- ISCCP 100 km)	0.12	45	0.89	7	0.92	445	491	53
CTP (ARM- LBTM nearest pixel)	0.07	19	0.78	90	0.92	445	489	66
CTP (ICARUS- LBTM nearest pixel)	0.07	13	0.83	71	0.88	476	489	40
CTP (ARM- LBTM 9 pixel avg)	0.10	−21	0.60	201	0.80	472	492	104
CTP (ICARUS- LBTM 9 pixel avg)	0.07	15	0.81	76	0.88	477	492	44
Log(Tau) (ARM-ISCCP 250 km)	0.21	−0.31	0.64	0.29	0.60	1.67	1.37	0.33
Log(Tau) (ARM-ISCCP 100 km)	0.20	−0.32	0.75	0.09	0.58	1.67	1.36	0.40
Log(Tau) (ARM-LBTM nearest pixel)	0.21	−0.55	0.68	0.18	0.63	1.68	1.32	0.32
Log(Tau) (ARM-LBTM 9 pixel avg)	0.18	−0.32	0.66	0.24	0.65	1.68	1.36	0.30

[a]The ISCCP data are averaged in 250 km and 100 km boxes centered on ARM SGP while the LBTM statistics are from the nearest pixel. Statistics are compiled during the year 2000 using the comparison criteria described in section 2.3. All CTP quantities are shown in mb while the Tau values are computed relative to $\log_{10}$(Tau).

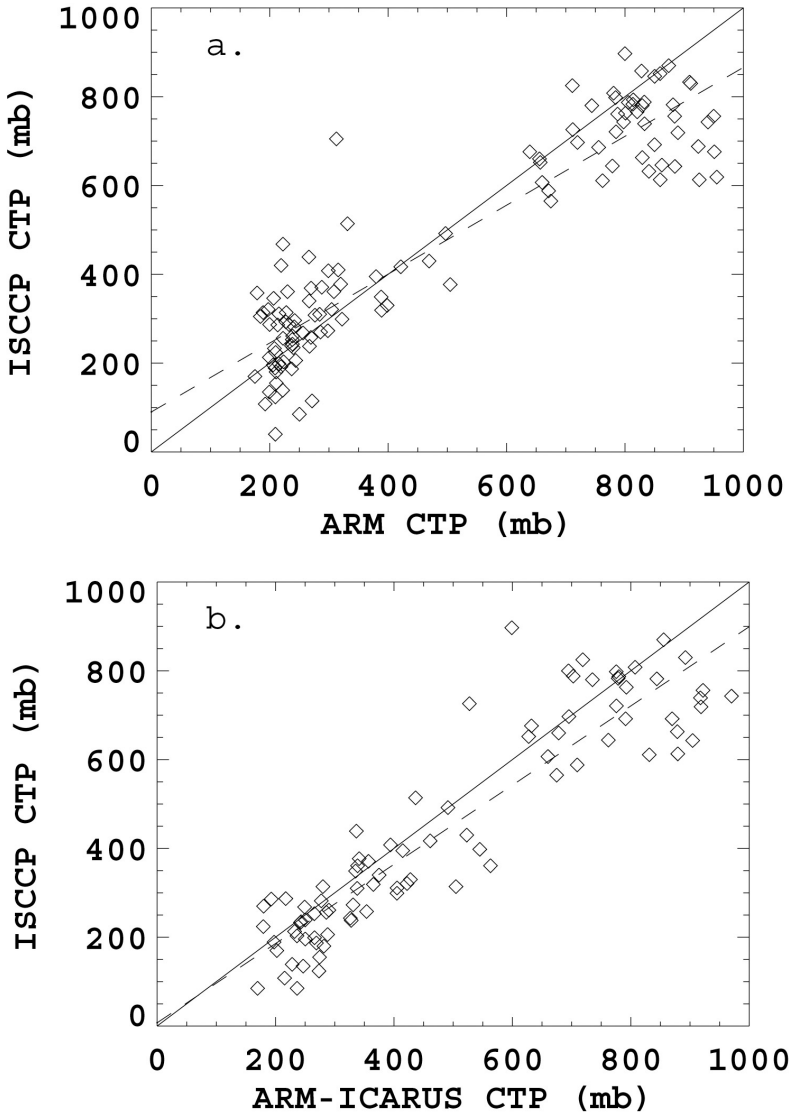

Figure 16. Comparison of ISCCP and LBTM quantities with ARM data. (a) CTP from ISCCP compiled in a 100 km domain centered on the SGP site, (b) as in Figure 16a except ISCCP is compared with ICARUS simulation using ARM data, (c) LBTM from the pixel nearest the ARM SGP site, (d) as in Figure 16c except LBTM is compared to the ICARUS simulation using ARM data, (e) ISCCP optical depth compared to the quantity derived from the ARM CPC diagnostic, and (f) as in Figure 16e except the LBTM nearest pixel optical depth is compared to ARM.

derived from the Kiehl et al. parameterization combined with the MMCR observed clouds and the supercooled LWP to parameterize a liquid water content profile. The IWC in mixed phase clouds is estimated from a new empirical relationship that is derived from a unique aircraft data set that includes measurements of both the particle size distribution and the IWC. Particle sizes are retrieved where possible and parameterized where retrieval algorithms are not applicable. To this microphysical description, standard radiative parameterizations are applied and the upwelling and downwelling solar and IR fluxes are calculated. Since we assume that the radar reflectivity contains condensed water content information, the algorithm is not applicable when precipitation contaminates the vertical profile. The occurrence of precipitation is diagnosed from the MWR brightness temperatures using an empirical algorithm described in the Appendix A and by the occurrence of a radar bright band in the MMCR profile of radar reflectivity.

[43] Validation of this scheme comes from various sources. We establish validity and uncertainty on the basis of flux closure at the surface and TOA. Summarized in Tables 5a and 5b, we find for the year 2000 in uniform overcast skies, that the calculations are strongly correlated to measurements with biases in the flux quantities at the surface and TOA of less than 10% and median fractional errors ranging from 20% to as low as 2%. We also compare our derived optical depths with optical depths derived from a technique using MFRSR that has itself been extensively validated [*Min and Harrison*, 1999]. In the optical depth comparison for uniform overcast skies during the year 2000

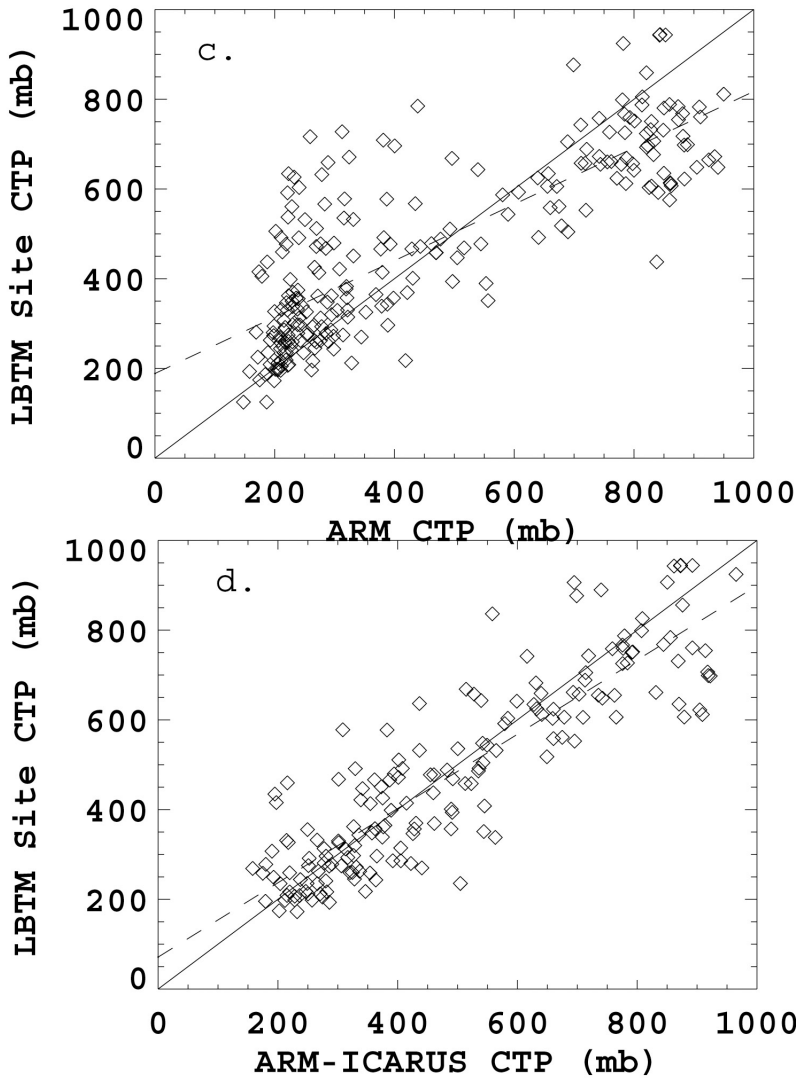

Figure 16. (continued)

(summarized in Table 3) we find that the comparison is essentially unbiased and highly correlated with a median fractional error of 20%. Most importantly, the high optical depth cases where the mixed phase parameterization is employed shows very good agreement with the MFRSR retrievals allowing us to have some confidence in the results of the column physical characterization (CPC) technique.

[44] As an initial application, we compared the results of the CPC with retrievals of cloud top pressure (CTP) and total column optical depth (τ_{tot}) produced by two satellite algorithms, ISCCP and LBTM. These satellite products are presently being used for evaluation of climate models. While the satellite products are correlated with the ground-based measurements, we find a decided tendency for the CTP to be biased into the middle troposphere for optically thin clouds and for the optical depths derived from the satellite algorithms to be underestimated. The tendency for the middle tropospheric CTP bias is largely mitigated by application of a satellite simulator algorithm (ICARUS [*Webb et al.*, 2001]). As for the findings of *Zhang et al.* [2005] who found that GCMs generally are producing too little middle level cloud and are biased high with respect to optical depth, our comparison suggests that these findings should be considered carefully in light of these results. In addition to an apparent low in the satellite algorithms at high optical depth, we also do not find the high frequency of middle tropospheric clouds of medium and low optical depth in the ground-based data that are reported by LBTM and ISCCP. Further analysis of the ARM data examining lidar observations for layers that might have been missed by the radar because of the detection threshold of the MMCR did not result in any significant changes to these findings. It seems clear that this issue should be examined more carefully before GCM parameterizations are adjusted with the intention of making the predicted optical depths come into agreement with ISCCP and LBTM.

[45] In addition to the satellite algorithm comparison, our findings from this work suggest that ground-based remote sensors can, with reasonable and quantifiable precision, characterize the physical properties of the atmospheric

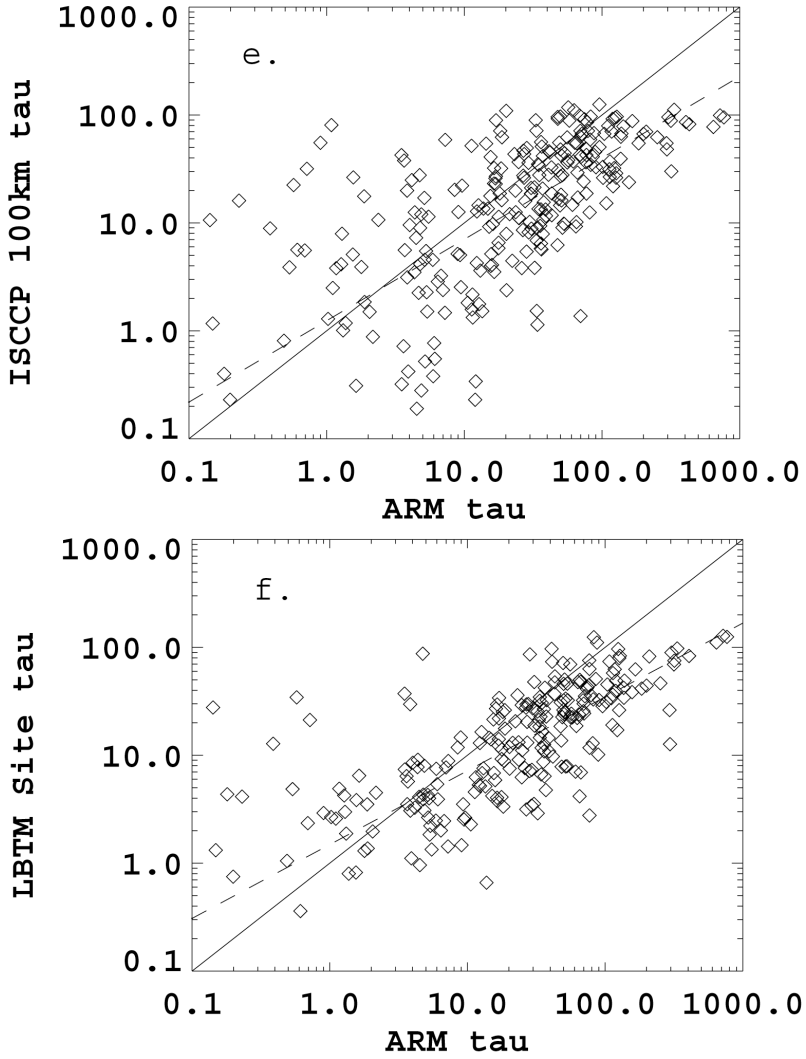

Figure 16. (continued)

column when using some combination of existing algorithms and parameterizations. In a companion paper (part 2) we show that heating within the atmosphere due to deposition of radiative flux in clouds can also be examined using long-term ground-based data. Given the simplicity of the diagnostic technique we apply to the ARM data, these results establish a baseline against which other more sophisticated algorithms can be compared; i.e., a metric. An algorithm designed to improve the characterization of microphysics so that the radiative properties of the column are more accurately or precisely estimated should be able to demonstrate measurable improvement in the boundary flux comparisons or in the total optical depth comparison shown here.

[46] Since the approach we have taken can be improved upon substantially with the use of more sophisticated cloud property retrieval algorithms, the fact that such simple schemes are able to describe the essential characteristics of the cloudy atmospheric column deserves comment. The ARM observations provide the basic quantities that constrain the atmospheric physical state, namely the vertical location of clouds and the total condensed liquid water. Along with the vertical distribution of Doppler radar observations in the ice phase parts of deep clouds, the observations seem to constrain the problem, even with the use of climatological or parameterized estimates of cloud particle size in the mixed phase clouds. One could argue that, to first order, the cloud location and total column water are what must be predicted by a GCM in order capture the essence of the radiative feedbacks by clouds and that the precise details of the cloud microphysics may be of secondary importance, at least relative to the present skill of climate models to predict cloud feedbacks [*Zhang et al.*, 2005].

Appendix A: Additional Initial Data Processing Details

[47] The initial data reduction that we conduct to enable the diagnostic analysis described in section 2 is an important component of our overall analysis procedure. In the following paragraphs, we describe the instruments, data streams, and methodologies that we have developed for this purpose.

A1. Microwave Radiometer

[48] The Microwave Radiometer (MWR) measures downwelling microwave radiation emitted from the sky at

23.8 GHz and 31.4 GHz from which the column integrated liquid and water vapor burdens are estimated. *Liljegren et al.* [2001] describes the features of the MWR used at the ARM sites and the data inversion algorithms that convert the microwave signals into condensed and vapor column amounts.

[49] One of the key issues in using the MWR is the need to avoid periods when precipitation is occurring or when the window in front of the microwave reflector is wet because of dew or precipitation that is ongoing or has recently ended. When the radome is wet, the MWR radiance measurements are biased by emission from the water on the radome (there is also an increase in MMCR noise due to emission by standing water on the MMCR radome). The period of radome drying after wetting by rain or dew is the most difficult problem since the timescale for drying depends on many variables including sunlight, wind, ambient humidity, and the degree of wetness of the radome. Therefore we have developed an empirical approach to identify wet radome events on the basis of the observed brightness temperature, outside air temperature, and sky imagery. Invoking the Rayleigh-Jeans law, we assume the brightness temperature measured by the MWR is linear with the emitting temperature of the water on the radome (taken as the outside air temperature), and a simple empirical formula is developed that predicts a threshold brightness temperature above which a wet radome could be expected. This threshold temperature was estimated by examining Total Sky Imager (TSI) images that document the presence of water on the silvered dome before and after cold and warm rain and noting the threshold brightness temperatures recorded by the MWR and the ambient outside air temperatures recorded by the Surface Meteorological Observing System (SMOS). A simple linear equation was then derived that predicts a threshold 31 GHz brightness temperature above which it is likely that the MWR radiance is contaminated by condensed water on the instrument. Our goal is simply to avoid wet radome periods in our long-term processing of ARM data and therefore we choose a reasonably conservative threshold. Figure 3 shows the time series of MWR brightness temperature, and retrieved liquid and vapor with the periods we estimate as wet during the 3-day case study period.

A2. Thermodynamic Profiles

[50] Since we seek to describe the state of the atmosphere at the SCF on a continuous basis over long periods of time, it is necessary to have an accurate and reasonably continuous description of the atmospheric thermodynamic state. Continuous thermodynamic profiles are required to help identify certain cloud types and to perform radiative transfer calculations. To accomplish this, we combine several sources of information regarding the thermodynamic state to generate what we have termed the merged sounding product. The thermodynamics profiles are ultimately defined on a 90 m height and 1 min time grid and consist of temperature, pressure, and water vapor mixing ratio. A 1-min time step was chosen because of the existence of 1-min averaged microwave radiometer retrievals of water vapor path.

[51] Sources of information for the merged sounding include radiosondes launched at the SCF, surface meteorological measurements from the ARM facility, MWR-derived precipitable water vapor, radiosondes launched from the Norman, Oklahoma National Weather Service (NWS) site, and mesoscale model output. Optimally, we prefer a continuously observed set of data of sufficient temporal and spatial detail to capture the evolution of the thermodynamic fields. This requires typically at least three hourly radiosonde profiles. Because of budgetary constraints, radiosondes have been launched on a somewhat irregular schedule at the SCF over the history of the ARM project. For example, during the middle and late 1990s, 3–5 soundings per day were launched from the SCF during regular daytime working hours Monday-Friday. No soundings were launched from the end of the workday on Friday until the first sounding early Monday morning. To maintain a continuous record, therefore, we augment the ARM soundings with the Norman NWS soundings (launched twice each day at 2330 and 1130 UTC), and, when the Norman soundings are not available, with the operational NCEP mesoscale model output from either the ETA or RUC models.

[52] The methodology we use for processing the radiosonde and model output data into a continuous time series is described by *Mace et al.* [1995]. Briefly, we begin with the radiosonde data files available in the ARM archive or the NWS files. These files generally contain several hundred to several thousand data points more or less equally spaced between the surface and the altitude where the balloon bursts. These data points are collected in the vertical bins where additional quality control is applied. The observations in each bin are then averaged. Account is also kept of the time of the observations in each vertical bin. A time grid is then defined (1 min) and the vertically averaged sounding data are linearly interpolated to it. When more than four hours exist between data points in any height bin, the profile is flagged as missing. Missing profiles are then filled by available Norman NWS soundings, RUC or ETA model soundings. Finally, since surface meteorological information is available at temporal resolutions of 1 min from the SMOS, we append the surface values to the range bin in the profile that corresponds to the surface. No effort is made to smooth the transitions between the observations from different sources, and these transitions are often quite noticeable in the time series plots. Account is kept, however, of what information contributes to a particular thermodynamic profile.

[53] Since a well-known upper tropospheric dry bias exists in the ARM radiosonde data [*Revercomb et al.*, 2003; *Turner et al.*, 2003], we apply the correction scheme reported by *Miloshevich et al.* [2001]. We then examine the MMCR data to identify where in each profile cloud is observed. In the cloudy bins, we force the relative humidity to be 100%. In regions warmer than freezing, we use the equilibrium vapor pressure with respect to pure water and at temperatures colder than 243 K we use the relative humidity with respect to pure ice. In the intermediate temperatures, a linear combination of the relative humidity with respect to ice and water is used. While the absolute value of the corrected mixing ratio profiles are questionable [*Soden et al.*, 2004], we rescale the mixing ratio profile on the basis of the 1-min averaged MWR-derived water vapor path. This straightforward technique assumes the shape of the mixing

ratio profile created by the linear interpolation procedure, the dry-bias correction, and the cloud occurrence correction faithfully represents the vertical distribution of water vapor in the column. The adjusted mixing ratio profile is converted to a weighting function and the MWR column integrated water vapor is distributed vertically according to this weighting function. This somewhat elaborate procedure is necessary because of the sensitivity of the longwave radiation to the vertical distribution of water vapor in the troposphere.

[54] The evolution of the moisture and temperature from 1 to 3 March is shown in Figure 4. The launch times of the 3-hourly soundings are shown as vertical lines in the height-time cross sections while the sounding data are shown compared to the Merged Sounding interpolation for each. We find the interpolated temperature is essentially indistinguishable from the measurement while the humidity diverges slightly from the measurement in the upper troposphere of several soundings. This apparent discrepancy is due to the fact that the sounding takes 30–40 min generally to reach the upper troposphere and we are comparing the Merged Sounding at the time of the launch, thus the small time offset between the actual measurement time and the interpolation time is enough to cause this difference in a rapidly changing water vapor field. While the humidity profiles shown in Figure 4b have not been scaled by the MWR vapor path, the values in the height time cross section have been. On the humidity cross section, we also show by the black symbols along the top of the diagram the diagnosis of precipitation using the empirical MWR technique described above. Besides the periods when the MWR is wet, two periods of anomalous humidity in the upper troposphere occurred near 2100–2200 UTC on 2 March and 0900–1000 UTC on 3 March in heavy cloud cover just after a period of light precipitation. The humidity sensor on the RS90 Sonde did not recover after leaving the cloud tops and continued to report high humidity into the stratosphere. This problem is reasonably well documented but is not captured by any quality control procedures currently in place.

A3. Millimeter Cloud Radar (MMCR)

[55] Since clouds are a key component of this observation-based strategy, profiles of cloud properties are needed as a function of height and time. The active cloud profiling instruments at the SCF are the millimeter cloud radar (MMCR), micropulse lidar (MPL) and the Raman lidar (RL). We use the MMCR primarily in this work. The MMCR is a vertically pointing Doppler radar operating at 35 GHz [*Moran et al.*, 1998]. The theory of cloud detection by millimeter radar is given by *Doviak and Zrnic* [1993] and *Clothiaux et al.* [1995] and, for the MMCR in particular in *Clothiaux et al.* [1999].

[56] The four MMCR data collection modes, optimized for various cloud types, run consecutively in a 36 s cycle. The cloud vertical profiles must be reconstructed from the modes in order to take advantage of the full capability of the MMCR data stream. Before this is accomplished, however, the significant radar echoes in the MMCR data profiles must be identified. Following the techniques described by *Clothiaux et al.* [1995] we have implemented cloud masking routines to identify this significant return in the MMCR profiles and then merge the modes into a single description of the Doppler moments in the vertical column. When merging the profiles, we depart from the technique described by *Clothiaux et al.* [2000] in that we do not perform interpolation to a 9 s temporal grid (the temporal spacing of the individual modes), instead we estimate the most reasonable measurements for a given 90 m vertical bin from one of the modes during the 36 s cycle and assign the three Doppler moment measurements from that particular mode to that bin. The temporal resolution of the merged radar Doppler moments product that we construct is then 36 s. Significant radar echoes from clouds are distinguished from insect and precipitation echoes in the boundary layer by using cloud base measurements recorded by ceilometers. The key differences between this radar product and the Active Remote Sensing by Clouds (ARSCL) product created operationally by ARM is the factor of 4 reduction in size of the data and a consistency between the radar reflectivity and the other two Doppler moments (velocity and spectral width).

Appendix B: A Relationship Between *IWC*, Z_e, and V_d

[57] We assume that the ice crystal size distribution can be approximated by an exponential function of the form $N(D) = N_0 \exp(-\lambda_e D)$ [*Heymsfield et al.*, 2002], and that power law relationships exist to describe the mass (m), cross-sectional area (A), radar backscatter, and ice crystal fall speed (V) in terms of the ice crystal maximum dimension (D):

$$m = a_m D^{b_m}, A = a_a D^{b_a}, V = a_v D^{b_v}, \frac{\sigma_b(D)\lambda^4}{D^6 \pi^5 |k_w|^2} = a_Z D^{b_Z}$$

where σ_b is the radar backscatter cross section, and we allow for the correction between the refractive indexes of ice and water (k_w) at the radar wavelength (λ) [*Mace et al.*, 2002]. *Mace et al.* [2002, equations (6) and (7)] can be integrated and rearranged to show that

$$Z_e = IWC \frac{a_z b_z}{a_m b_m} \frac{\Gamma\{b_z\}}{\Gamma\{b_m\}} \left(\frac{b_m + 1}{D_{mass}}\right)^{b_m - b_Z} \tag{B1}$$

$$\overline{V}_d = a_v \left(\frac{b_m + 1}{D_{mass}}\right)^{-b_v} \left(1 + \frac{b_v}{b_Z}\right) \frac{\Gamma\{b_z + b_v\}}{\Gamma\{b_z\}} \tag{B2}$$

where Γ is the gamma function and D_{mass} is the mass weighted maximum dimension. Eliminating D_{mass} in equations (B1) and (B2), we can write, $IWC = C\, Z_e\, \overline{V}_d^{\alpha}$ where C and α depend only on the power law coefficients.

[58] **Acknowledgments.** Funding for this work was provided by the Environmental Science Division of the U.S. Department of Energy (grant DE-FG0398ER657). Data were obtained from the Atmospheric Radiation Measurement Program sponsored by the U. S. Department of Energy, Office of Science, Office of Biological and Environmental Research, Environmental Science Division. S.K. is supported by a NASA grant of the Clouds and the Earth's Radiant Energy System (CERES) project grant (NNL04AA26G). The UND Citation aircraft operations were supported

under Department of Energy/Pacific Northwest National Laboratory grant 354794-A-Q8.

References

Ackerman, T. P., and G. M. Stokes (2003), The Atmospheric Radiation Measurement program, *Phys. Today*, *56*, 38–45.

Atlas, D., S. Y. Matrosov, A. J. Heymsfield, M.-D. Chou, and D. B. Wolff (1995), Radar and radiation properties of ice clouds, *J. Appl. Meteorol.*, *34*, 2329–2345.

Barnard, J. C., J. C. Doran, S. Zhong, and C. N. Long (2001), A comparison of cloud properties at Barrow and SHEBA during the summer of 1998, paper presented at 11th Atmospheric Radiation Measurement Science Team Meeting, U.S. Dep. of Energy, Atlanta, Ga., March.

Clothiaux, E. E., M. A. Miller, B. A. Albrecth, T. P. Ackerman, J. Verlinde, D. M. Babb, R. M. Peters, and W. J. Syrett (1995), An evaluation of a 94 GHz radar for remote sensing of cloud properties, *J. Atmos. Oceanic Technol.*, *12*, 201–229.

Clothiaux, E. E., K. P. Moran, B. E. Martner, T. P. Ackerman, G. G. Mace, T. Uttah, J. H. Mather, K. B. Widener, M. A. Miller, and D. J. Rodriguez (1999), The Atmospheric Radiation Measurement program cloud radars: Operational modes, *J. Atmos. Oceanic Technol.*, *16*, 819–827.

Clothiaux, E. E., T. P. Ackerman, G. G. Mace, K. P. Moran, R. T. Marchand, M. A. Miller, and B. E. Martner (2000), Objective determination of cloud heights and radar reflectivities using a combination of active remote sensors at the ARM CART sites, *J. Appl. Meteorol.*, *39*, 645–665.

Dong, X., and G. G. Mace (2003), Profiles of low-level stratus cloud microphysics deduced from ground-based measurements, *J. Atmos. Oceanic Technol.*, *20*, 45–53.

Dong, X., P. Minnis, G. G. Mace, W. L. Smith, M. Poellot, R. T. Marchand, and A. D. Rapp (2002), Comparison of stratus cloud properties derived from surface, GOES, and aircraft data during the March 2000 ARM cloud IOP, *J. Atmos. Sci.*, *59*, 3265–3284.

Doviak, R. J., and D. S. Zrnic (1993), *Doppler Radar and Weather Observations*, 2nd ed., Elsevier, New York.

Frisch, A. C., W. Fairall, and J. B. Snider (1995), Measurement of stratus cloud and drizzle parameters in ASTEX with a K-band Doppler radar and a microwave radiometer, *J. Atmos. Sci.*, *52*, 2788–2799.

Frisch, A. C., G. Feingold, W. Fairall, and T. Uttal (1998), On cloud radar and microwave radiometer measurements of stratus cloud liquid water profiles, *J. Geophys. Res.*, *103*, 23,195–23,197.

Fu, Q. (1996), An accurate parameterization of the solar radiative properties of cirrus clouds for climate models, *J. Clim.*, *9*, 2058–2082.

Fu, Q., P. Yang, and W. B. Sun (1998), An accurate parameterization of the infrared radiative properties of cirrus clouds for climate models, *J. Clim.*, *9*, 2223–2237.

Heymsfield, A. J. (1972), Ice crystal terminal velocities, *J. Atmos. Sci.*, *29*, 1348–1357.

Heymsfield, A. J. (1977), Precipitation development in stratiform ice clouds, *J. Atmos. Sci.*, *34*, 367–381.

Heymsfield, A. J., and C. M. R. Platt (1984), A parameterization of the particle size spectrum of ice cloud in terms of the ambient temperature and ice water content, *J. Atmos. Sci.*, *41*, 846–855.

Heymsfield, A. J., S. Lewis, A. Bansemer, J. Iaquinta, L. M. Miloshevich, M. Kajikawa, C. Twohy, and M. R. Poellot (2002), A general approach for deriving the properties of cirrus and stratiform ice cloud particles, *J. Atmos. Sci.*, *59*, 3–30.

Kato, S., T. P. Ackerman, J. H. Mather, and E. E. Clothiaux (1999), The k-distribution method and correlated-k approximation for a Shortwave Radiative Transfer Model, *J. Quant. Spectrosc. Radiat. Transfer*, *62*, 109–121.

Kato, S., G. L. Smith, and H. W. Barker (2001), Gamma-weighted discrete ordinate two-stream approximation for computation of domain-averaged solar irradiance, *J. Atmos. Sci.*, *58*, 3797–3803.

Khaiyer, M. M., A. D. Rapp, P. Minnis, D. R. Doelling, W. L. Smith Jr., L. Nguyen, M. L. Nordeen, and Q. Min (2002), Evaluation of a 5-year cloud and radiative property dataset derived from GOES-8 data over the southern Great Plains, paper presented at 12th Atmospheric Radiation Measurement Science Team Meeting, U.S. Dep. of Energy, St. Petersburg, Fla., 8–12 April. (Available at http://www.arm.gov/publications/proceedings/conf12/extended_abs/khaiyer-mm.pdf)

Kiehl, J., J. Hack, G. B. Bonan, B. A. Boville, D. L. Williamson, and P. J. Rasch (1998), The National Center for Atmospheric Research Community Climate Model: CCM3, *J. Clim.*, *11*, 1131–1149.

Liljegren, J. C., E. E. Clothiaux, G. G. Mace, S. Kato, and X. Dong (2001), A new retrieval for cloud liquid water path using a ground-based microwave radiometer and measurements of cloud temperature, *J. Geophys. Res.*, *106*(D13), 14,485–14,500.

Liou, K. N. (1974), Analytic two-stream and four-stream solutions for radiative transfer, *J. Atmos. Sci.*, *31*, 1473–1475.

Liu, C., and A. J. Illingworth (2000), Toward more accurate retrievals of ice water content from radar measurements of clouds, *J. Appl. Meteorol.*, *39*, 1130–1146.

Long, C. N., and T. P. Ackerman (2000), Identification of clear skies from broadband pyranometer measurements and calculation of downwelling shortwave cloud effects, *J. Geophys. Res.*, *105*, 15,609–15,626.

Mace, G. G., and K. Sassen (2000), A constrained algorithm for retrieval of stratocumulus cloud properties using solar radiation, microwave radiometer and millimeter cloud radar data, *J. Geophys. Res.*, *105*, 29,099–29,108.

Mace, G. G., D. O'C. Starr, T. P. Ackerman, and P. Minnis (1995), Examination of coupling between an upper tropospheric cloud system and synoptic scale dynamics diagnosed from wind profiler and radiosonde data, *J. Atmos. Sci.*, *52*, 4094–4127.

Mace, G. G., T. P. Ackerman, P. Minnis, and D. F. Young (1998), Cirrus layer microphysical properties derived from surface-based millimeter radar and infrared interferometer data, *J. Geophys. Res.*, *103*, 23,207–23,216.

Mace, G. G., E. E. Clothiaux, and T. P. Ackerman (2001), The composite characteristics of cirrus clouds: Bulk properties revealed by 1-year of continuous cloud radar data, *J. Clim.*, *14*, 2185–2203.

Mace, G. G., A. J. Heymsfield, and M. R. Poellot (2002), On retrieving the microphysical properties of cirrus clouds using the moments of the millimeter-wavelength Doppler spectrum, *J. Geophys. Res.*, *107*(D24), 4815, doi:10.1029/2001JD001308.

Mace, G. G., Y. Zhang, S. Platnick, M. D. King, P. Minnis, and P. Yang (2005), Evaluation of cirrus cloud properties derived from MODIS radiances using cloud properties derived from ground-based data collected at the ARM SGP site, *J. Appl. Meteorol.*, *44*, 221–240.

Mace, G. G., S. Benson, and S. Kato (2006), Cloud radiative forcing at the Atmospheric Radiation Measurement Program Climate Research Facility: 2. Vertical redistribution of radiant energy by clouds, *J. Geophys. Res.*, *111*, D11S91, doi:10.1029/2005JD005922.

Matrosov, S. Y., B. W. Orr, R. A. Kropfli, and J. B. Snider (1994), Retrieval of vertical profiles of cirrus cloud microphysical parameters from Doppler radar and infrared radiometer measurements, *J. Appl. Meteorol.*, *33*, 617–626.

Miloshevich, L. M., H. Vomel, A. Paukkunen, A. J. Heymsfield, and S. J. Oltmans (2001), Characterization and correction of relative humidity measurements from Vaisala Rs80A radiosondes at cold temperatures, *J. Atmos. Oceanic Technol.*, *18*, 135–155.

Min, Q., and L. C. Harrison (1996a), Cloud properties derived from surface MFRSR measurements and comparison with GOES results at the ARM SGP site, *Geophys. Res. Lett.*, *23*(13), 1641–1644.

Min, Q., and L. C. Harrison (1996b), An adjoint formulation of the radiative transfer method, *J. Geophys. Res.*, *101*(D1), 1635–1640.

Min, Q.-L., and L. C. Harrison (1998), Comparison of model-predicted total shortwave with measurements under overcast cloud conditions, paper presented at Eighth Atmospheric Radiation Measurement Science Team Meeting, U.S. Dep. of Energy, Tucson, Ariz.

Min, Q., and L. Harrison (1999), Joint statistics of photon pathlength and cloud optical depth, *Geophys. Res. Lett.*, *26*(10), 1425–1428.

Min, Q.-L., M. Duan, and R. Marchand (2003), Validation of surface retrieved cloud optical properties with in situ measurements at the Atmospheric Radiation Measurement Program (ARM) South Great Plains site, *J. Geophys. Res.*, *108*(D17), 4547, doi:10.1029/2003JD003385.

Min, Q.-L., E. Joseph, and M. Duan (2004), Retrievals of thin cloud optical depth from a multifilter rotating shadowband radiometer, *J. Geophys. Res.*, *109*, D02201, doi:10.1029/2003JD003964.

Minnis, P., and W. L. Smith Jr. (1998), Cloud and radiative fields derived from GOES-8 during SUCCESS and the ARM-UAV spring 1996 flight series, *Geophys. Res. Lett.*, *25*, 1113–1116.

Minnis, P., P. W. Heck, and D. F. Young (1993), Inference of cirrus cloud properties using satellite-observed visible and infrared radiances, part II: Verification of theoretical cirrus radiative properties, *J. Atmos. Sci.*, *50*, 1305–1322.

Minnis, P., W. L. Smith Jr., D. P. Garber, J. K. Ayers, and D. R. Doelling (1995), Cloud properties derived from GOES-7 for the spring 1994 ARM Intensive Observing Period using version 1.0.0 of the ARM satellite data analysis program, *NASA Ref. Publ. 1366*, 59 pp.

Minnis, P., L. Nguyen, D. R. Doelling, D. F. Young, W. F. Miller, and D. P. Kratz (2002), Rapid calibration of operational and research meteorological satellite imagers, part I: Evaluation of research satellite visible channels as references, *J. Atmos. Oceanic Technol.*, *19*, 1233–1249.

Mitchell, D. L. (1996), Use of mass- and area-dimensional power laws for determining precipitation particle terminal velocities, *J. Atmos. Sci.*, *53*, 1710–1723.

Mitchell, D. L., and A. J. Heymsfield (2005), Refinements in the treatment of ice particle terminal velocities, highlighting aggregates, *J. Atmos. Sci.*, *62*, 1637–1645.

Mlawer, E. J., S. J. Taubman, P. D. Brown, M. J. Iacono, and S. A. Clough (1997), Radiative transfer for inhomogeneous atmospheres: RRTM, a validated correlated-k model for the longwave, *J. Geophys. Res.*, *102*, 16,663–16,682.

Moran, K. P., B. E. Marner, M. J. Post, R. A. Kropfli, D. C. Welsh, and K. B. Widener (1998), An unattended cloud-profiling radar for use in climate research, *Bull. Am. Meteorol. Soc.*, *79*, 443–455.

Peixoto, J. P., and A. Oort (1993), *The Physics of Climate*, 520 pp., Am. Inst. of Phys., New York.

Randall, D. A. (1995), Editorial: Atlantic Stratocumulus Transition Experiment, *J. Atmos. Sci.*, *52*, 2705–2706.

Randall, D. A., B. A. Albrecht, S. K. Cox, P. Minnis, W. Rossow, and D. Starr (1995), On FIRE at ten, *Adv. Geophys.*, *38*, 37–177.

Revercomb, H. E., et al. (2003), The Atmospheric Radiation Measurement Program's water vapor intensive observation periods: Overview, initial accomplishments, and future challenges, *Bull. Am. Meteorol. Soc.*, *84*, 217–236.

Rossow, W. B., and R. A. Schiffer (1991), ISCCP cloud data products, *Bull. Am. Meteorol. Soc.*, *72*, 2–20.

Rossow, W. B., and R. A. Schiffer (1999), Advances in understanding clouds from ISCCP, *Bull. Am. Meteorol. Soc.*, *80*, 2261–2288.

Rossow, W. B., and T.-C. Zhang (1995), Calculation of surface and top of atmosphere radiative fluxes from physical quantities based on ISCCP data sets: 2. Validation and first results, *J. Geophys. Res.*, *100*, 1167–1197.

Slingo, J. M. (1989), A GCM parameterization for the shortwave radiative properties of water clouds, *J. Atmos. Sci.*, *46*, 1419–1427.

Soden, B. J., D. D. Turner, B. M. Lesht, and L. M. Miloshevich (2004), An analysis of satellite, radiosonde, and lidar observations of upper tropospheric water vapor from the Atmospheric Radiation Measurement Program, *J. Geophys. Res.*, *109*, D04105, doi:10.1029/2003JD003828.

Stephens, G. L. (1995), Editorial: The First ISCCP Regional Experiment Intensive Field Observations II, *J. Atmos. Sci.*, *52*, 4041.

Stokes, G. M., and S. E. Schwartz (1994), The atmospheric radiation measurement (ARM) program: Programmatic background and design of the cloud and radiation testbed, *Bull. Am. Meteorol. Soc.*, *75*, 1201–1221.

Toon, O. B., C. P. McKay, T. P. Ackerman, and K. Santhanam (1989), Rapid calculation of radiative heating rates and photodissociation rates in inhomogeneous multiple scattering atmospheres, *J. Geophys. Res.*, *94*(D13), 16,287–16,301.

Turner, D. D., B. M. Lesht, S. A. Clough, J. C. Liljegren, H. E. Revercomb, and D. C. Tobin (2003), Dry bias and variability in Vaisala radiosondes: The ARM experience, *J. Atmos. Oceanic. Technol.*, *20*, 117–132.

Twohy, C. H., A. J. Schanot, and W. A. Cooper (1997), Measurement of condensed water content in liquid and ice clouds using an airborne counterflow virtual impactor, *J. Atmos. Oceanic. Technol.*, *14*, 197–202.

Webb, M., C. Senior, S. Bony, and J. J. Morcrette (2001), Combining ERBE and ISCCP data to assess clouds in the Hadley Centre, ECMWF and LMD atmospheric climate models, *Clim. Dyn.*, *17*, 905–922.

Wielicki, B. A., et al. (1998), Clouds and the Earth's Radiant Energy System (CERES): Algorithm overview, *IEEE Trans. Geosci. Remote Sens.*, *36*, 1127–1141.

Zhang, M. H., et al. (2005), Comparing clouds and their seasonal variations in 10 atmospheric general circulation models with satellite measurements, *J. Geophys. Res.*, *110*, D15S02, doi:10.1029/2004JD005021.

S. Benson, G. G. Mace, and Q. Zhang, Department of Meteorology, University of Utah, Salt Lake City, UT 84112-0110, USA. (mace@met.utah.edu)

D. R. Doelling, Analytical Services and Materials, Inc., One Enterprise Parkway, Suite 300, Hampton, VA 23666-5845, USA.

X. Dong and M. Poellot, Department of Atmospheric Sciences, University of North Dakota, Grand Forks, ND 58202, USA.

S. Kato, Center for Atmospheric Sciences, Hampton University, Hampton, VA 23668, USA.

C. Long, Pacific Northwest National Laboratory, Richland, WA 99352, USA.

Q. Min, Atmospheric Sciences Research Center, 251 Fuller Road, Albany, NY 12203, USA.

P. Minnis, NASA Langley Research Center, Hampton, VA 23681, USA.

K. L. Sonntag, Cooperative Institute for Mesoscale Meteorological Studies, University of Oklahoma, Norman, OK 73019, USA.

C. H. Twohy, College of Oceanic and Atmospheric Sciences, Oregon State University, Corvallis, OR 97331-4501, USA.